

T.C. Johns · J.M. Gregory · W.J. Ingram
C.E. Johnson · A. Jones · J.A. Lowe
J.F.B. Mitchell · D.L. Roberts · D.M.H. Sexton
D.S. Stevenson · S.F.B. Tett · M.J. Woodage

Anthropogenic climate change for 1860 to 2100 simulated with the HadCM3 model under updated emissions scenarios

Received: 29 April 2002 / Accepted: 31 October 2002 / Published online: 18 February 2003
© Springer-Verlag 2003

Abstract In this study we examine the anthropogenically forced climate response over the historical period, 1860 to present, and projected response to 2100, using updated emissions scenarios and an improved coupled model (HadCM3) that does not use flux adjustments. We concentrate on four new Special Report on Emission Scenarios (SRES) namely (A1FI, A2, B2, B1) prepared for the Intergovernmental Panel on Climate Change Third Assessment Report, considered more self-consistent in their socio-economic and emissions structure, and therefore more policy relevant, than older scenarios like IS92a. We include an interactive model representation of the anthropogenic sulfur cycle and both direct and indirect forcings from sulfate aerosols, but omit the second indirect forcing effect through cloud lifetimes. The modelled first indirect forcing effect through cloud droplet size is near the centre of the IPCC uncertainty range. We also model variations in tropospheric and stratospheric ozone. Greenhouse gas-forced climate change response in B2 resembles patterns in IS92a but is smaller. Sulfate aerosol and ozone forcing substantially modulates the response, cooling the land, particularly northern mid-latitudes, and altering the monsoon structure. By 2100, global mean warming in SRES scenarios ranges from 2.6 to 5.3 K above 1900 and precipitation rises by 1%/K through the twenty first century (1.4%/K omitting aerosol changes). Large-scale patterns of response broadly resemble those in an earlier model (HadCM2), but with important regional differences, particularly in the tropics. Some divergence in future response occurs across scenarios for the regions

considered, but marked drying in the mid-USA and southern Europe and significantly wetter conditions for South Asia, in June–July–August, are robust and significant.

1 Introduction

There is growing expectation that increases in the concentrations of greenhouse gases arising from human activity will lead to substantial changes in climate in the twenty first century. Indeed, there is already evidence that anthropogenic emissions of greenhouse gases (GHGs) have altered the large-scale patterns of temperature over the twentieth century (Santer et al. 1996; Tett et al. 1999; Barnett et al. 1999; Stott et al. 2001; Mitchell et al. 2001), although natural factors, including changes in solar output and episodic volcanic emissions, may also have contributed. Future climate change will probably be dominated by the response to anthropogenic forcing factors. Large uncertainties remain, however, in the expected anthropogenic climate response, partly through model uncertainty in the projected climate sensitivity to increasing GHGs and partly as a result of both physical and modelling uncertainties in the amplitude and geographical patterns of non-GHG forcings which modulate this GHG-forced response (particularly from sulfate aerosol indirect cooling effects).

The main motivation for the present study is to provide up-to-date estimates of global climate change suitable for deriving impacts assessments on regional scales with self-consistent scenario assumptions. Even though some of the regional details may be unreliable, this approach at least gives a picture of possible consequences of alternative future emissions scenarios, derived in a physically consistent way, which can be interpreted for policymakers in the context of negotiations to limit emissions so as to prevent 'dangerous' climate change.

T.C. Johns (✉) · J.M. Gregory · W.J. Ingram · C.E. Johnson
A. Jones · J.A. Lowe · J.F.B. Mitchell · D.L. Roberts
D.M.H. Sexton · S.F.B. Tett · M.J. Woodage
Met Office, Hadley Centre for Climate Prediction and Research,
London Road, Bracknell, RG12 2SY, UK
E-mail: tim.johns@metoffice.com

D.S. Stevenson
Department of Meteorology, University of Edinburgh King's
Buildings, Edinburgh EH9 3JZ, Scotland, UK,

Some questions that arise are whether GHG-induced warming (determined by global average emissions) will dominate, or whether local sulfate aerosol forcing (much more dependent on local emissions) will be a significant factor over the twenty first century and, if the latter, what differences in the regional responses might be expected under different emissions scenarios? Could non-linear climate-chemistry feedbacks become increasingly important to consider in future, with an implication of added importance attached to the details of alternative emissions pathways that result in similar time-integrated emissions? To tackle such questions it is important that there should be consistency and some plausibility about the emissions scenarios used to force climate models. The IPCC SRES ('Special Report on Emissions Scenarios', Nakicenovic et al. 2000) marker scenarios developed in conjunction with the IPCC Third Assessment Report, have been developed specifically to provide more self-consistent and up-to-date scenarios for climate modelling than hitherto. We have therefore primarily adopted these in the present study, though we also refer back to the older IS92a scenario which has already been used extensively in climate impact studies (e.g. US National Assessment Report 2000; Hulme et al. 1999; Hulme and Jenkins 1998).

Given emission scenarios of GHGs, sulfur and other anthropogenic precursor gases, understanding the climate sensitivity to the resulting anthropogenic forcings and the interactions between climate change, atmospheric chemistry feedbacks and transport processes is still a major challenge. Coupled climate models including representations of the relevant physical, dynamical and chemical processes are an essential tool, not just for making predictions but for increasing understanding of the feedbacks and sensitivities. Here we use a state-of-the-art coupled climate model (HadCM3, Gordon et al. 2000) incorporating an explicit sulfur cycle to predict anthropogenic sulfate burdens from emissions and including the anthropogenic forcing effects thought to be most relevant at the moment, applied in a way as consistent with the emissions scenario as possible. The results therefore represent plausible estimates of global climate change consequent upon the socio-economic assumptions underlying the emissions scenarios.

The structure is as follows: in the next section we document the version of the coupled model used in the study and the physical basis for calculating the anthropogenic forcings. In Sect. 3 we briefly outline the performance of the model in a long control integration with no anthropogenic forcing imposed. Then in Sect. 4 we outline the anthropogenically forced experiments, with a fuller description of the emissions, concentrations and forcing scenarios in Sect. 5. In Sect. 6 we examine the modelled future climate response and regional variations in the various forcing scenarios, assessing them in the light of previous model studies and exploring the questions posed. Some final conclusions, caveats and future outlook are presented in Sect. 7.

2 Model description

The HadCM3 coupled model (Gordon et al. 2000) is used in the simulations. HadCM3 was developed from the earlier HadCM2 model (Johns et al. 1997), but various improvements to the atmosphere and ocean components mean that it needs no artificial flux adjustments to prevent excessive climate drift. The atmosphere and ocean exchange information once per day, heat and water fluxes being conserved exactly. Momentum fluxes are interpolated between atmosphere and ocean grids so are not conserved precisely, but this non-conservation is not thought to have a significant effect.

2.1 Atmosphere

The atmospheric component of the model, HadAM3 (Pope et al. 2000), has 19 levels with a horizontal resolution of 2.5° latitude by 3.75° longitude, comparable to a spectral resolution of T42.

A new radiation scheme is included with six spectral bands in the shortwave and eight in the longwave. The radiative effects of minor greenhouse gases as well as CO_2 , water vapour and ozone are explicitly represented (Edwards and Slingo 1996). A simple parametrization of background aerosol (Cusack et al. 1998) is also included.

A new land surface scheme (Cox et al. 1999) includes a representation of the freezing and melting of soil moisture, as well as surface runoff and soil drainage; the formulation of evapotranspiration includes the dependence of stomatal resistance on temperature, vapour pressure and CO_2 concentration. The surface albedo is a function of snow depth, vegetation type and also of temperature over snow and ice.

A penetrative convective scheme (Gregory and Rowntree 1990) is used, modified to include an explicit downdraught and the direct impact of convection on momentum (Gregory et al. 1997). Parametrizations of orographic and gravity wave drag have been revised to model the effects of anisotropic orography, high drag states, flow blocking and trapped lee waves (Milton and Wilson 1996; Gregory et al. 1998). The large-scale precipitation and cloud scheme is formulated in terms of an explicit cloud water variable following Smith (1990). The effective radius of cloud droplets is a function of cloud water content and droplet number concentration (Martin et al. 1994).

2.2 Ocean and sea ice

The oceanic component of the model has 20 levels with a horizontal resolution of $1.25^\circ \times 1.25^\circ$. At this resolution it is possible to represent important details in oceanic current structures (Wood et al. 1999).

Horizontal mixing of tracers uses a version of the adiabatic diffusion scheme of Gent and McWilliams (1990) with a variable thickness diffusion parametrization (Wright 1997; Visbeck et al. 1997). There is no explicit horizontal diffusion of tracers. The along-isopycnal diffusivity of tracers is $1000 \text{ m}^2/\text{s}$ and horizontal momentum viscosity varies with latitude between 3000 and $6000 \text{ m}^2/\text{s}$ at the poles and equator respectively.

Near-surface vertical mixing is parametrized by a Kraus-Turner mixed layer scheme for tracers (Kraus and Turner 1967), and a K-theory scheme (Pacanowski and Philander 1981) for momentum. Below the upper layers the vertical diffusivity is an increasing function of depth only. Convective adjustment is modified in the region of the Denmark Straits and Iceland-Scotland ridge better to represent down-slope mixing of the overflow water, which is allowed to find its proper level of neutral buoyancy rather than mixing vertically with surrounding water masses. The scheme is based on Roether et al. (1994).

Mediterranean water is partially mixed with Atlantic water across the Strait of Gibraltar as a simple representation of water mass exchange since the channel is not resolved in the model.

The sea-ice model uses a simple thermodynamic scheme including leads and snow-cover. Ice is advected by the surface ocean current, with convergence prevented when the depth exceeds 4 m (Cattle and Crossley 1995).

There is no explicit representation of iceberg calving, so a prescribed water flux is returned to the ocean at a rate calibrated to balance the net snowfall accumulation on the ice sheets, geographically distributed within regions where icebergs are found. In order to avoid a global average salinity drift, surface water fluxes are converted to surface salinity fluxes using a constant reference salinity of 35 PSU.

2.3 Sulfur cycle and sulfate aerosols

In addition to the improvements mentioned in existing physical schemes, HadAM3 also now includes the capability to model the transport, chemistry and physical removal processes of anthropogenic sulfate aerosol which is input to the model in the form of surface and high level emissions of SO₂ (outlined later; a fuller description of the interactive sulfur cycle in the model may be found in Jones et al. 1999). Note that this is in contrast to some earlier climate model studies (e.g. Mitchell and Johns 1997), which only included sulfate aerosol effects based on prescribed burdens. Other recent climate change studies including an interactive sulfur cycle include Roeckner et al. (1999) and Boville et al. (2001).

Sulfur dioxide (SO₂), dimethyl sulfide (DMS) and three modes of sulfate aerosol can be represented explicitly in terms of mass-mixing ratio as prognostic variables in HadAM3. There are two size modes of free sulfate particle, both assumed to have lognormal size distributions; the Aitken mode has (number) median radius 24 nm and geometric standard deviation $\sigma_{ait} = 1.45$, and the accumulation mode has median radius 95 nm and $\sigma_{acc} = 1.4$. The third mode represents sulfate dissolved in cloud droplets. The variables are advected horizontally and vertically using a positive definite tracer advection scheme (distinct from the advection scheme used for the atmospheric prognostic variables), and also transported in the vertical by the convection scheme. Turbulent mixing in the boundary layer is parametrized in a way similar to that of heat and moisture, with the allowance for injection of SO₂ (anthropogenic or volcanic) and DMS emissions at appropriate levels, and dry deposition of SO₂ and sulfate species at the surface. SO₂ is converted to the sulfate modes in a chemistry routine included in the model, which parametrizes the gas and aqueous phase oxidation reactions using monthly mean 3-dimensional oxidant fields (OH, H₂O₂ and HO₂) from the STOCHEM Lagrangian chemistry model (Collins et al. 1997), HO₂ being used to regenerate hydrogen peroxide. The oxidant distributions used in the experiments described later were derived from a STOCHEM run appropriate for present-day conditions (Stevenson et al. 2000). The following transfers between the sulfate modes are also parametrized: evaporation of dissolved sulfate to form accumulation mode, nucleation of accumulation mode sulfate to form dissolved sulfate, and diffusion of Aitken mode sulfate into cloud droplets. Wet scavenging of SO₂ and the sulfate modes is parametrized in the model's large-scale precipitation and convection schemes.

The Aitken and accumulation sulfate modes are used in the radiation code to simulate their direct effect on the Earth's radiation budget; that is, the direct scattering or absorption of incoming solar radiation by the aerosol particles. For this purpose, the particles are assumed to be composed of a mixture of ammonium sulfate and water, the refractive indices of ammonium sulfate at selected wavelengths being taken from Toon et al. (1976). The particles are assumed to be spherical, so that Mie theory can be used to calculate the scattering and absorption coefficients. This is done separately for the Aitken and accumulation modes, which are assigned the lognormal size distributions as mentioned. However these are the distributions of the dry particles; for radiative purposes the hygroscopic growth of the particles is taken into account so that their effective sizes are often larger, by an amount that depends on the relative humidity in the model. The growth function is based partly on the parametrization of Fitzgerald (1975), which

has the convenient property that the size distribution of the moist aerosol continues to be lognormal. It should be noted that Mie theory calculations are not performed during the model integration, but beforehand; the results are supplied to the model in the form of look-up tables of aerosol single scattering parameters for both the Aitken and accumulation modes.

To estimate the indirect effect of sulfate aerosols on the radiative properties of clouds account must be taken of the fact that cloud droplet number concentrations (N_d) in the HadCM3 control run are set to fixed values of 600 cm⁻³ over land and 150 cm⁻³ over ocean (Bower and Choullarton 1992). Another consideration is the fact that the HadCM3 experiments only consider anthropogenic SO₂ emissions. Consequently, data from separate runs of the sulfur-cycle model embedded in HadAM3 were used to parametrize the indirect effect on cloud albedo for subsequent use in the climate change experiments, as detailed in Sect. 5 and Appendix A. Note that the effect of sulfate aerosols on cloud precipitation efficiency, the 'second indirect' or 'lifetime' effect (Albrecht 1989) is not modelled in this study.

3 Control simulation

The coupled model is initialized directly from the Levitus observed ocean state (Levitus and Boyer 1994; Levitus et al. 1995) at rest, with a suitable atmospheric and sea-ice state. There is no spinup with surface or interior ocean relaxation, the model runs freely from the start. A long control integration (CTL) with fixed forcing representing late nineteenth century conditions was performed providing initial conditions for the climate change simulations. This run has recently been extended to over 2000 years.

The global-mean annual surface air temperature (Fig. 1) shows only a very small trend of -0.011 K/century over the first 2000 years, smaller in magnitude than the trend in the previous HadCM2 model (Johns et al. 1997), despite HadCM3 not using flux adjustments or any initial spinup procedure. A slight, almost linear, drift of atmospheric mass also occurs, amounting to a reduction in mean surface pressure of about -0.244 hPa/century over the first 1000 years; a correction was applied at 1310 years to prevent any further drift.

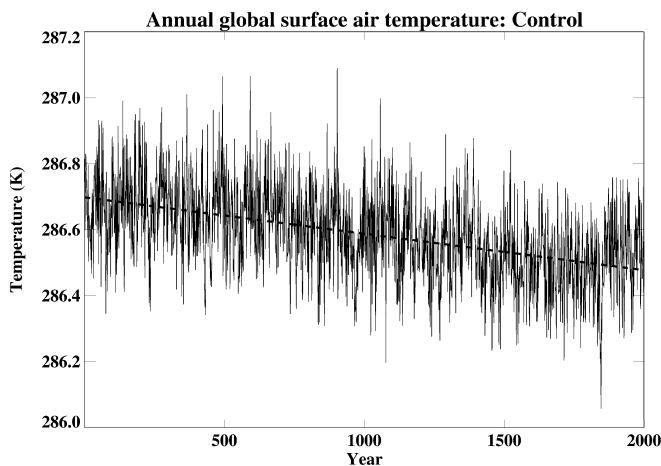


Fig. 1 Time series of annual global mean surface air temperature over the first 2000 years of the HadCM3 control simulation. The best fit linear trend is the *dashed line*

HadCM3 is not the only model to get very small surface drifts without flux adjustments. Such a result was previously obtained by Boville and Gent (1998) and (with smaller subsurface drifts) by Boville et al. (2001). However, those simulations were much shorter than the HadCM3 control and employed an elaborate spinup procedure.

3.1 Mean climatology and variability

Gordon et al. (2000) describe some of the main features of the first 400 years of the control simulation, concentrating on the global heat budget, ocean and sea-ice climatology. Although some temporal drift is apparent in the deeper ocean in its water masses and circulation, the ocean surface climatology is highly stable and generally well simulated, making the model suitable for the long climate change experiments reported here.

Seasonal mean atmospheric circulation patterns can be judged from Fig. 2, which may also be compared with HadCM2 (Fig. 10 of Johns et al. 1997). Overall the simulation is good; probably an improvement over HadCM2 in the Southern Hemisphere thanks to higher pressure in the subtropical anticyclones and reduced depth of the Antarctic circumpolar trough. In the Northern Hemisphere, HadCM3's main error is that the Icelandic low is too shallow and the gradient too slack in the Atlantic storm track region in DJF, an error similar to but somewhat worse than HadCM2. The North Pacific storm track perhaps extends too far to the east

compared to the analyses. Pressure is considerably too high in JJA and particularly DJF over the Arctic, with correspondingly rather low pressure over Asia in DJF. The Asian monsoon trough is well captured in the model, however, as are the subtropical ocean high pressure systems.

In general, the model does a good job of capturing the patterns of mean seasonal precipitation for DJF and JJA when judged against the CMAP climatology (Xie and Arkin 1997), illustrated in Fig. 3 and 4. At most latitudes modelled zonal mean global precipitation corresponds closely with CMAP in both seasons. The agreement over land (Fig. 3c, d), where the climatology is more reliable, is particularly good, giving confidence in the model physics. The split zonal-mean maximum in the tropics in DJF and strong peak in JJA are reproduced quite well (Fig. 3a, b), though in JJA the model tends to shift the peak precipitation slightly equatorwards and there is rather a split ITCZ (inter-tropical convergence zone) response over the W Pacific ocean (Figs. 3f, 4b), a common problem in coupled models. While the modelled zonal mean precipitation over the Southern Ocean appears rather high (Fig. 3e, f), the CMAP reconstruction here is subject to larger uncertainty; the agreement is better in southern summer when observations are more abundant.

More detailed examination of the precipitation distribution (Fig. 4) supports the view that the model is generally realistic, but some deficiencies are apparent. In both seasons the model tends to overdo the precipitation in the eastern tropical Atlantic/Gulf of Guinea,

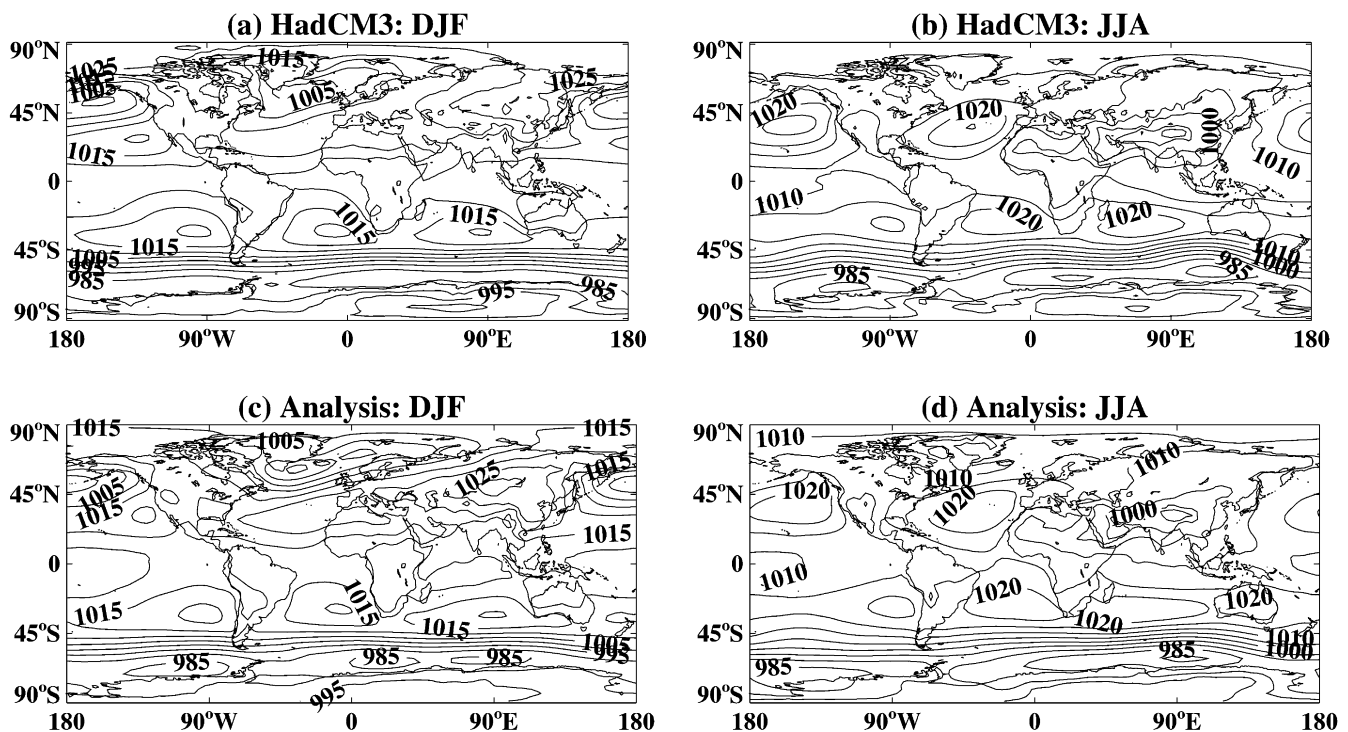
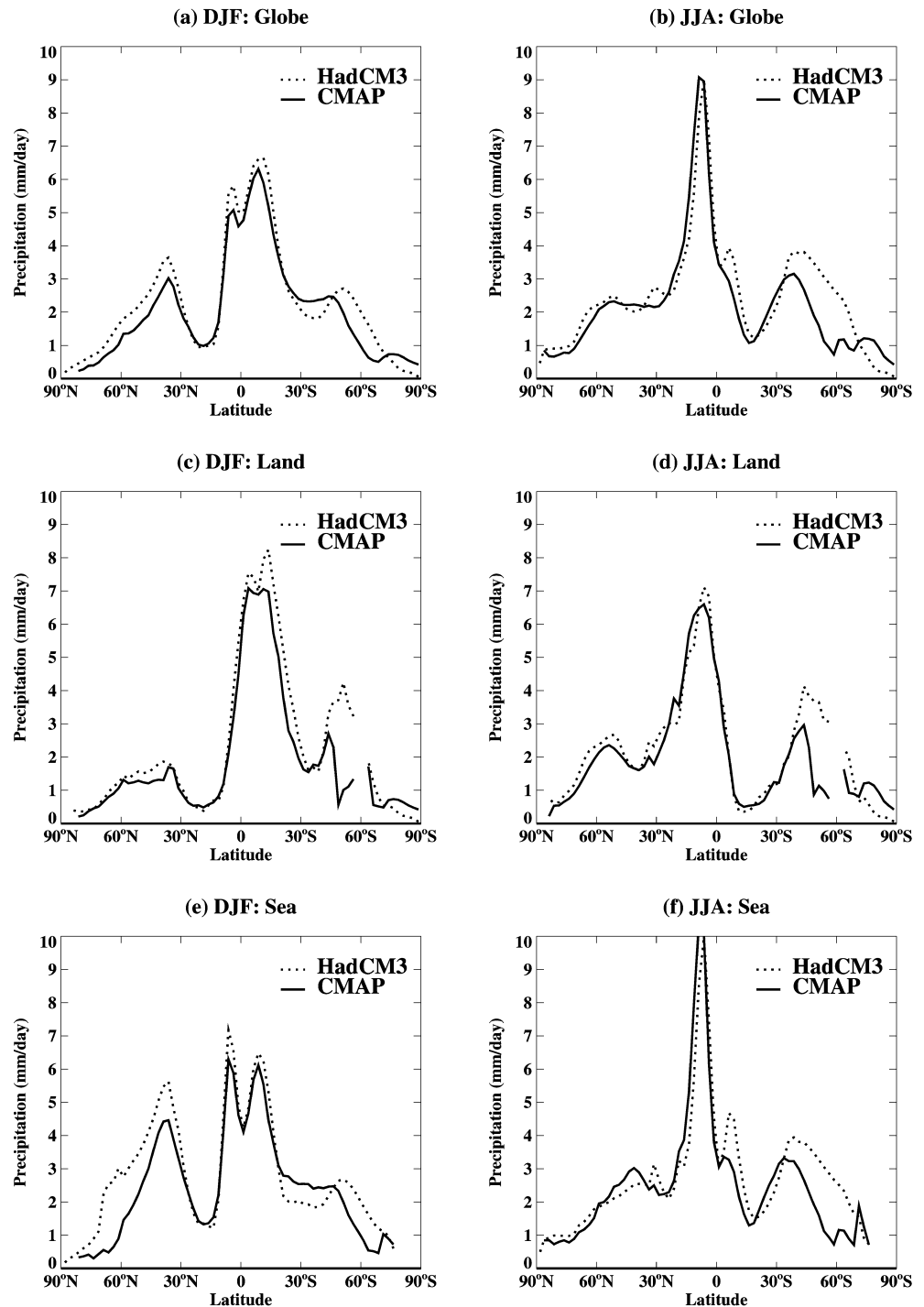


Fig. 2a–d Seasonal average (DJF and JJA) mean sea level pressure (hPa) simulated for years 371–610 in the HadCM3 control run, compared with mean UK Meteorological Office operational analyses for the period May 1983 to September 1995

Fig. 3a–f Zonal seasonal average (DJF and JJA) precipitation (mm/day) as simulated in the HadCM3 control run for the same period as in Fig. 2 compared to the CMAP climatology (Xie and Arkin 1997), for the globe, land and sea separately



probably because local warm SST (sea surface temperature) errors (Gordon et al. 2000) enhance convection. In JJA particularly this tends to broaden the ITCZ too much here. Related to this, the model is rather deficient in precipitation in JJA over tropical South America.

Detailed consideration of the realism of modes of variability in the model is outside the scope of this study, but Collins et al. (2001) show that ENSO-like tropical variability exhibited by the model is reasonably realistic in structure and amplitude, with better teleconnection patterns than in the previous model, and that the

HadCM3 control run's variability patterns in the Northern Hemisphere winter can be related quite well to the observed behaviour of the North Atlantic/Arctic oscillations.

4 Anthropogenically forced experiments

The following experiments including time-varying anthropogenic forcings have been performed with HadCM3:

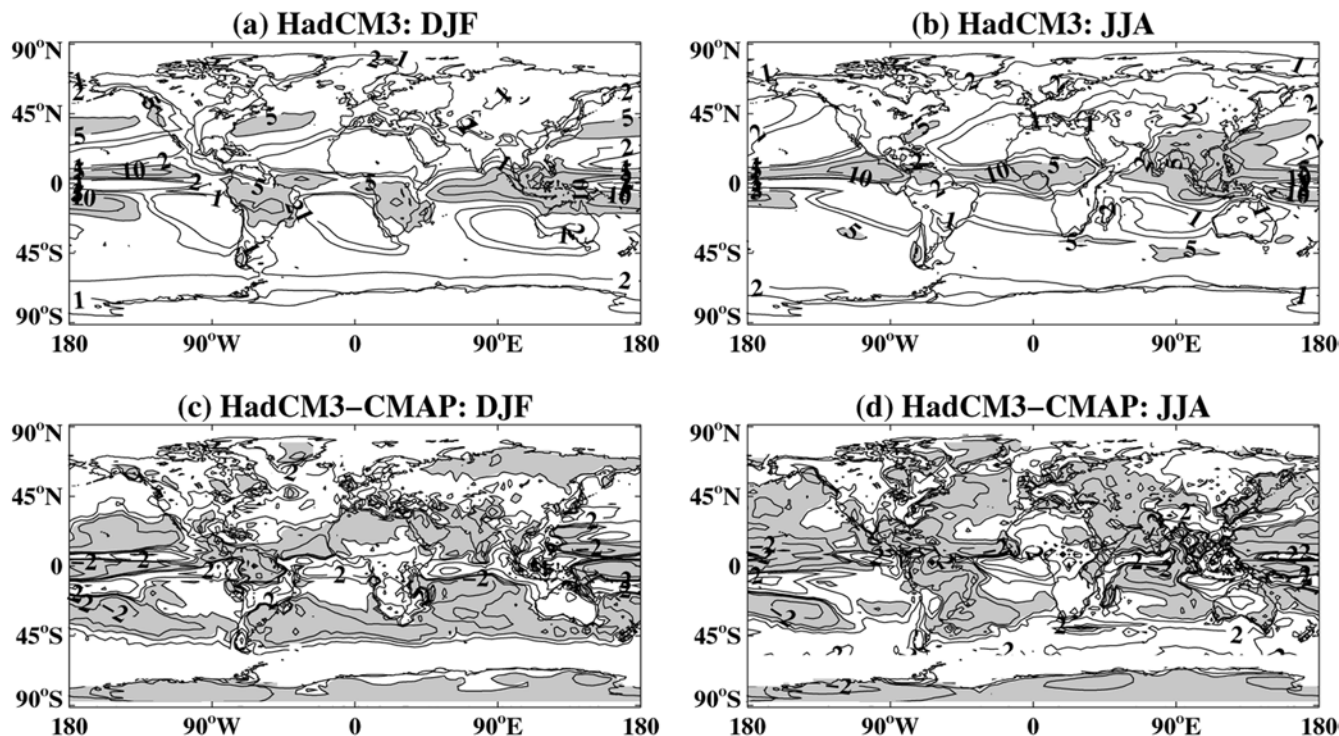


Fig. 4a, b Seasonal average (DJF and JJA) precipitation in the HadCM3 control run for the same period as in Fig. 2 (contours at 1, 2, 5, 10, 20 mm/day; values above 5 mm/day *shaded*), and **c, d** differences relative to the CMAP climatology (Xie and Arkin 1997) (contours at $-5, -2, -0.5, 0, 0.5, 2, 5$ mm/day; negative values *shaded*)

1. G92, forcing from observed rises in well-mixed GHGs (WMGHGs) only from 1859 to present-day, thereafter the IS92a scenario for WMGHGs up to 2100
2. A92, forcing from rises in WMGHGs as in G92, plus estimates of past changes in tropospheric ozone concentration and sulfur emissions, extended from 1990 to 2100 according to an adapted scenario loosely based on IS92a emissions
3. GB2, as G92, with forcing due to WMGHGs only but using the B2 scenario after 1990 instead of IS92a
4. A1FI, A2, B2, B1, forcing changes from observed rises in WMGHGs to present as G92 plus estimates of past changes in tropospheric and stratospheric ozone concentration and sulfur emissions, extended from 1990 to 2100 according to SRES A1FI, A2, B2 and B1 scenarios (Nakicenovic et al. 2000) with estimated/modelled stratospheric ozone recovery

G92 was initialized from year 100 of the control run, A1FI and B1 from year 470, while the remaining experiments were initialized from year 370. A1FI and B1 are identical experiments up to 1989, and similarly A2 and B2.

Results from the A92 experiment can be obtained from the IPCC Data Distribution Centre website at <http://ipcc-ddc.cru.uea.ac.uk/>, where it is referred to as the HC3AA integration, but as the scenario is not standard it is not discussed further in this study. We con-

centrate here on the other six experiments: G92, GB2, A1FI, A2, B2 and B1, particularly the four SRES cases.

A number of research groups have recently carried out SRES scenario experiments (mostly the A2 and B2 cases) with other coupled models (Stendel et al. 2000; Dai et al. 2001; Noda et al. 2001; Nozawa et al. 2001; Mahlman 2001); results from these as well as the present study are summarized in the IPCC 2001 report (Cubasch et al. 2001).

5 Emissions, concentrations and radiative forcings

5.1 Well-mixed greenhouse gases

Concentration data for ‘well-mixed greenhouse gases’ are input separately to the model for the three principal gases CO_2 , CH_4 and N_2O , and also for a subset of the halocarbon species estimated to be the next largest contributors to anthropogenic radiative forcing in the recent past and next 100 years. These were CFCl_3 (“CFC-11”), CF_2Cl_2 (“CFC-12”), $\text{CF}_2\text{ClCFCl}_2$ (“CFC-113”), CHF_2Cl (“HCFC-22”), CF_3CFH_2 (“HFC-134a”) and C_2HF_5 (“HFC-125”). They were assumed to have zero concentration until 1950, 1950, 1980, 1970, 1990 and 1990 respectively, with histories before 1990 taken from Table 2.5 of Shine et al. 1990. Note that, unlike some other models (e.g. CSM; Boville et al. 2001) that do represent their spatial variation, we regard all

these species as completely well mixed for convenience, although some actually have significant variations over the model domain (at least in the stratosphere).

For the historical period, CO₂, CH₄ and N₂O were as specified in the IPCC 1995 report (Schimel et al. 1996; T. Wigley personal communication) based on calculations with the Bern model (Joos et al. 1996).

For the future scenario part of the experiments CH₄, HFCs and HCFC-22 concentrations were calculated from a continuous run of an updated version of a 2-D chemistry transport model (“TROPOS”) used by Hough (1991). This model runs with fixed transport, and climatologies for temperature and humidity. It was driven using SRES A1FI, A2, B2 and B1 scenario emissions (Nakicenovic et al. 2000) together with estimates of natural emissions for methane from IPCC 1995 (Schimel et al. 1996), while CO₂ and N₂O data were supplied from sources working in the SRES scenario development process (M. Prather personal communication). We adjusted output GHG values slightly near 2000 to match observational estimates and avoid discontinuity with the historical part of the scenario. In the G92 experiment, concentration values for GHGs after 1990 were instead taken directly from IPCC 1995 (Tables 2.5d, 2.5e in Schimel et al. 1996). CFCs and other chlorine and bromine-containing compounds were calculated in a box model to give CFC concentrations and the time-dependent effective chlorine loading of the troposphere.

The GHG concentration data used to drive the A1FI, A2, B2/GB2 and B1 scenario experiments are summarized in Table 1a, b. G92 differs from these only slightly up to 1990.

The total GHG forcing at 2000 relative to pre-industrial is about 2.34 W/m² in the B2 experiment (and similar in others), towards the lower end of the IPCC estimated range (Table 3a). Of this, 65% comes from CO₂ and 35% from ‘minor’ gases, CFCs and other halocarbons accounting for about 12%. In the future, the fractional contribution of minor GHGs falls significantly, to 22% and 21% in A2 and B2 respectively by 2100, by which time the halocarbon contribution to the total GHG forcing (which spans a range of 7.94 W/m² for A1FI down to 4.22 W/m² for B1; Table 3b) is even smaller (around 5% or less), although the absolute forcing from halocarbons shows little change.

The total change in radiative heating from 2000 to 2100 for those WMGHGs included is within about 0.1 W/m² of the sum of the values given in Ramaswamy et al. (2001). The small difference arises from a combination of slight discrepancies between the concentrations of GHGs used in the model compared to the IPCC estimates for the present-day period, the use of a preliminary version of the SRES emissions scenarios (as was the case for other studies in the IPCC 2001 Report), and different radiation schemes used to calculate the implied forcings.

Table 1a Greenhouse gas concentrations input to the model versus simulated year, for the historical period 1859–1990 followed by the SRES A2 scenario. Entries left blank and intermediate years are linearly interpolated from the given data points

Year	CO ₂ (ppmv)	CH ₄ (ppbv)	N ₂ O (ppbv)	CFC-11 (pptv)	CFC-12 (pptv)	CFC-113 (pptv)	HCFC-22 (pptv)	HFC-125 (pptv)	HFC-134A (pptv)
1859	286.1	878	280.1	0	0	0	0	0	0
1875	288.8								
1890	294.3	947							
1900	295.9								
1917	302.2								
1920		1032							
1935	309.6								
1940		1098							
1950	310.9		290.0	0	0				
1957		1191							
1960	316.9			18	30				
1965			294.2						
1970	325.7			60	120		0		
1980	338.9			173		0			
1984			303.7						
1990	351.1	1718	310	263	477	77	91	0	0
1995	358.1								
1998				262	533	83			
2000	366.8	1762	318	251	523	81	165	2	34
2010	388.4	1874	327	206	474	72	188	5	94
2020	415.4	2012	338	169	430	64	151	10	168
2030	448.9	2170	351	138	389	57	110	16	237
2040	486.3	2353	364	113	353	51	85	23	283
2050	526.9	2559	378	93	320	45	68	32	333
2060	571.6	2783	392	76	290	40	31	42	456
2070	620.9	3026	407	62	263	36	15	53	585
2080	676.7	3295	422	51	239	32	8	66	735
2090	741.9	3593	439	42	216	28	4	81	914
2100	818.9	3927	455	34	196	25	2	99	1134

1b. As Table 1a, but for the SRES B1, B2 and A1FI scenarios 1990–2100. Note that the CFC concentrations are identical to A2 in all these scenarios so are omitted in this table

	Year	CO ₂ (ppmv)	CH ₄ (ppbv)	N ₂ O (ppbv)	HCFC22 (pptv)	HFC125 (pptv)	HFC134A (pptv)
B1	1990	351.1	1700	308	97	0	1
	1995	358.2					
	2000	367	1754	316	172	1	20
	2010	386.5	1813	324	250	3	62
	2020	409	1869	334	215	9	116
	2030	433	1896	342	131	17	171
	2040	457.7	1883	350	81	25	229
	2050	481.9	1844	358	44	34	300
	2060	501.7	1809	365	19	43	357
	2070	515.8	1781	369	8	49	385
	2080	524.2	1734	373	3	53	398
2090	529.8	1672	376	1	56	401	
2100	531.4	1594	377	1	58	394	
B2	1990	351.1	1718	310	91	0	0
	1995	358.1					
	2000	366.8	1745	318	164	2	35
	2010	387.9	1821	327	188	6	98
	2020	410.7	1927	335	150	11	168
	2030	433	2041	342	100	19	259
	2040	454.8	2165	347	52	27	357
	2050	476.9	2299	352	24	38	474
	2060	499.5	2395	356	11	49	587
	2070	523.2	2445	358	5	60	684
	2080	547.9	2476	361	2	70	777
2090	574.8	2499	362	1	80	873	
2100	603.7	2521	364	0.5	90	977	
A1FI	1990	351.1	1700	308	97	0	1
	1995	358.1					
	2000	366.4	1707	316	172	1	20
	2010	386.9	1763	325	249	3	65
	2020	414	1874	336	215	11	138
	2030	450.5	2048	348	132	23	248
	2040	497.5	2277	363	84	38	370
	2050	556	2528	381	47	56	517
	2060	623	2730	399	21	75	659
	2070	694.5	2884	416	9	92	758
	2080	770.8	3025	433	4	105	810
2090	848.5	3155	449	2	116	832	
2100	925.5	3263	465	1	123	829	

5.2 Tropospheric and stratospheric ozone

Tropospheric and stratospheric ozone trends are calculated separately as zonal averages on the model levels, trends from one epoch to another being linearly extrapolated and added to a baseline climatology following Li and Shine (1995) but with a number of alterations. The more significant alterations are intended to represent “pre-industrial” conditions (the 1960s and early 1970s, not 1765 as conventional for other gases) by filling in the Antarctic ozone hole and elsewhere applying smaller changes based on SAGE (Stratospheric Aerosol and Gas Experiment) data (Wang et al. 1996). Future concentrations of stratospheric ozone were estimated assuming chlorine and bromine emissions decrease as set out in the Montreal Protocol. Tropospheric ozone concentrations were calculated using runs of the three-dimensional global chemical transport model STOCHEM (Collins et al. 1997, 1999) to derive interpolated trends over the experimental period. Appendix B gives further details of the methodology used to

compute the tropospheric and stratospheric ozone trends (see also Tett et al. 2002). Climate change can affect ozone predictions (Johnson et al. 1999; Stevenson et al. 2000). For the A2 and B2 scenarios only, this is allowed for approximately by using future climates, derived from the HadCM3 G92 run, in STOCHEM. This was not the case for A1FI, the 1989–90 (i.e. present day) climate from the B2 run being used instead, in order to make the forcing in A1FI more similar to corresponding experiments being conducted by other modelling groups. Further details of natural emissions etc. are described in Stevenson et al. (2000).

The estimated changes in radiative forcing in the model from 2000 to 2100 due to changes in tropospheric ozone are much smaller than the estimates given by Ramaswamy et al. (2001) (e.g. 0.18 compared to 0.87 W/m² for A2). There are several reasons for this. STOCHEM gave about a 15% smaller change in tropospheric ozone abundances for A2 than the values used by Ramaswamy et al. (2001); see also Prather et al. (2001). In addition, the ozone concentrations in Prather

et al. (2001) are thought to be about 25–30% too high (due to an error they included a contribution from increases in stratospheric ozone). In the B2 and A2 scenarios, the calculations here, unlike those in Prather et al. (2001), took into account changes in temperature and humidity estimated from an earlier climate change experiment (see earlier), further reducing the concentrations, see Johnson et al. (2001). The net effect is that the change in radiative forcing due to changes in tropospheric ozone from 2000 to 2100 in Prather et al. (2001) may be an overestimate by about a factor of two. However, there is a further reduction in the contribution to the discrepancy arising from the interpolation of ozone changes from STOCHEM onto the coarser vertical resolution of HadCM3, in which changes at the tropopause were set to zero. Due to the discretization and interpolation of trends in the vertical, the result was to reduce the ozone changes immediately below the tropopause, precisely the region in which changes would have their strongest radiative effect (Forster and Shine 1997). Thus the values here are about 0.2 W/m^2 in the A2 and A1FI scenarios, smaller than the Prather et al. (2001) values, even allowing for the possible shortcomings in their estimate.

To evaluate the implied forcing from imposed ozone changes presents some difficulties in that the radiative forcing concept relates to the flux change at the tropopause, but ozone depletion at and above this level causes potentially strong adjustments in stratospheric temperatures system ownward longwave (LW) flux at the tropopause. The adjustment of the stratosphere to an instantaneous change of ozone would take place on a time-scale of a few months and one should let these adjustments reach equilibrium before evaluating the implied forcing on the troposphere and climate system below.

In this study, we calculated the forcing by two alternative methods. Our preferred method is to calculate the forcing interactively in the coupled model by making double calls to the radiation scheme with both the evolving state and a reference control (unperturbed) state (Tett et al. 2002), and estimating the forcing as the difference between the two radiative calculations at the diagnosed tropopause averaged over a few years of model integration. We used this method for the years 2000, 2050 and 2100 when the stratospheric ozone changes are most significant.

The alternative method of estimating ozone forcing involves first calculating the stratospheric radiative heating/cooling rates using the control run (unperturbed forcing), assuming the stratosphere to be in radiative and dynamical balance. We here assume that under imposed ozone changes the dynamical changes are negligible. Hence to maintain equilibrium, radiative heating rates must also remain unchanged. To achieve this, iterative calculations were performed off-line from the model experiments themselves, in which stratospheric temperatures were adjusted under the imposed ozone changes until the radiative heating rates return to

the reference values. This method is referred to as the ‘fixed dynamical heating’ (FDH) approximation (e.g. Ramanathan and Dickinson 1979). Ozone distributions for selected years of the coupled model experiments were iterated using this method for monthly mean states from a two year section of the control run and the radiative flux changes at the tropopause averaged over the two years to derive the approximated radiative forcing in the experiments. We used this method for the years 1900, 1950, 1975, 1990, 2000, 2050 and 2100, allowing us to compare with the interactive method, and also allowing direct comparison with earlier studies that used the FDH method.

The FDH approximation could be unrealistic if significant dynamical adjustments also occur in the stratosphere in response to ozone changes. We can judge this to some extent by examining the radiative and dynamical balance in the forced experiments themselves (see Sect. 6), although other forcings and feedbacks may amplify or reduce these dynamical changes.

Our preferred method of calculating the ozone forcing interactively (Tett et al. 2002) appears to yield a higher cooling effect from stratospheric ozone depletion than the FDH method and therefore a lower net warming effect overall in general (Table 3c). However, the difference between the two forcing estimates is at most a few tenths of a W/m^2 in the A1FI, A2, B2 and B1 scenarios throughout the twenty first century, a minor uncertainty relative to the total forcing.

5.3 Sulfur and sulfate aerosols

As mentioned in Sect. 2, the direct radiative effect of sulfate aerosols is determined explicitly from the anthropogenic aerosol concentration and physical state of the atmosphere. The effect is computed in both the clear-sky and cloudy portions of a grid box but is much less significant in the presence of cloud.

To determine the indirect sulfate forcing effect, a more complex calibration procedure was required as described in Appendix A. The anthropogenic forcing changes were applied in the HadCM3 experiments via specified cloud albedo perturbations based on prior calibration experiments performed separately using HadAM3, which had the natural and anthropogenic emissions included with present-day climate. This method avoids the need to include the natural sulfur cycle explicitly in the control and forced HadCM3 experiments, which would have been more expensive computationally. The technique produces an indirect aerosol forcing distribution in HadCM3 similar to that in the HadAM3 calibration runs but typically of about 70% of the magnitude, the discrepancy arising from at least three sources:

1. Limitations of the parametrized method; e.g. running into limits on the cloud effective radius, and so being unable to produce the desired amount of forcing, and

the fact that the simple measure of cloud albedo used may not accurately track the (complex) changes in cloud radiative properties which actually produce the forcing.

- Problems with time-averaging such that the forcing associated with timestep-by-timestep changes in cloud albedo (as in the HadAM3 calibration runs) is not the same as that produced by an annual-mean of these albedo changes (as used in the HadCM3 experiments).
- Differences in the meteorology in the simulations, particularly in the distribution of clouds which will produce differences in the forcing locally.

Given the large uncertainty in estimates of the indirect effect (e.g. Ramaswamy et al. 2001), this imperfect method was nevertheless considered adequate for this study.

The variations in sulfate aerosol burdens and forcings in A1FI, A2, B2 and B1 are illustrated in

Fig. 5, with linear interpolation between the calibration years which are marked with symbols. One year re-runs were performed with additional radiation computations to derive these forcings. The global annual mean (anthropogenic) aerosol burden at 2000 is approximately 0.25 Tg(S), from emissions of 69 Tg(S) per annum, implying a burden/emissions ratio of 1.32 days. This ratio is clearly too low; for example the average of the same ratio among 11 models tabulated by Penner et al. (2001) is 2.9 days. The main reason for the low aerosol loading is that the rates of dry and wet deposition are too rapid in this version of the model. However, it is also relevant that anthropogenic sulfur emissions produce less aerosol (per unit mass of S emitted) than natural emissions, for reasons discussed by Penner et al. (2001), who quoted a range of 0.8 to 2.9 days for this ratio with respect to anthropogenic SO₂ emissions.

In accordance with the emissions scenarios, the global-mean burden and forcing both rise sharply in

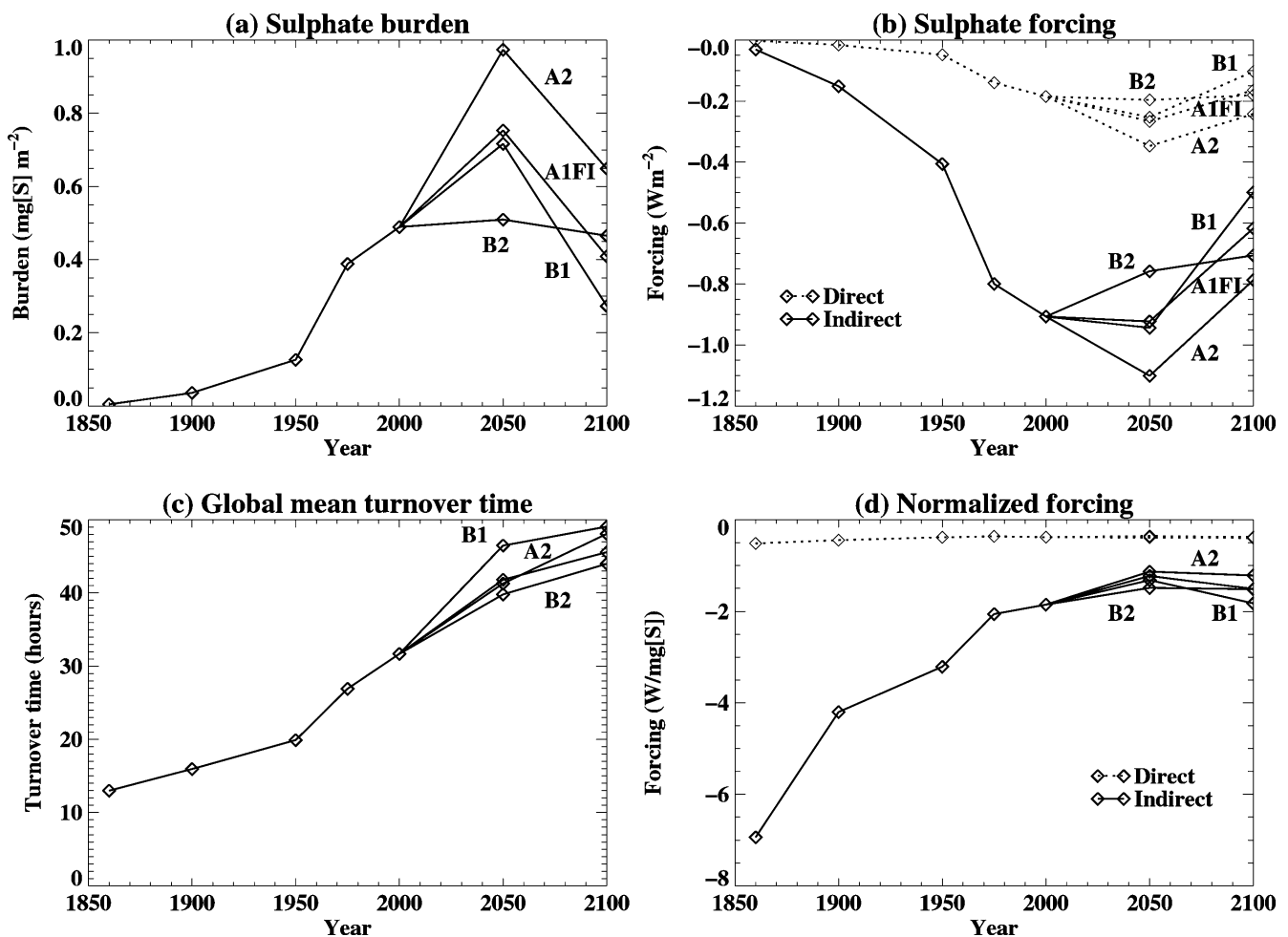


Fig. 5 Time series of **a** global mean anthropogenic sulfate burden; **b** direct and indirect sulfate forcing; **c** global annual mean turnover time in the atmosphere (i.e. anthropogenic sulfur burden divided by emissions); and **d** normalized direct and indirect forcing (i.e. forcing divided by burden); for the A1FI, A2, B2 and B1 experiments. Note

that the forcings and burdens represent data computed from single years of the experiments only, not continuously throughout the simulations. The indirect forcing as diagnosed in the coupled experiments is typically about 30% weaker than that diagnosed in separate offline calculations using HadAM3 (see text)

A1FI and A2, peaking at 2030 (between the 2000 and 2050 data points plotted in Fig. 5) before falling back at 2100. (Regional breakdowns of the anthropogenic sulfur emissions in the A1FI, A2, B2 and B1 scenarios by broad world economic regions are given in Table 2). The global burden in B2 (Fig. 5a) remains quite level over the twenty first century despite a marked decrease in emissions from 69.0 to 47.3 Tg[S]/year between 2000 and 2100, and in A2 the burden at 2100 is considerably

higher than 2000 despite the reduced emissions (60.3 Tg[S]/year at 2100).

A pronounced rise in the effective global mean turnover time is thus apparent through the simulations (Fig. 5c). The most significant factor is the migration through time of emissions to subtropical and tropical regions where oxidant concentrations are much greater than in mid-latitudes and therefore more efficient for sulfate production – the rise is a consequence primarily

Table 2 Sulfur emissions (Mt(S)/year) by world economic regions at decadal intervals for the preliminary SRES scenarios B2 and A2 (Steve Smith personal communication), and the B1 marker and A1FI illustrative scenarios (Nakicenovic et al. 2000)

	Year	OECD 90	FSU/EE = REF	China/CPA + SE Asia = ASIA	Lat Am + Afr/Mid E = ALM	Shipping	Total
B1	1990	22.7	<i>17.0</i>	<i>17.7</i>	<i>10.5</i>	3.0	<i>70.9</i>
	2000	17	11.0	25.3	12.8	3.0	69.0
	2010	11.8	9.0	29.0	21.2	3.0	73.9
	2020	7.9	7.7	29.1	26.8	3.0	74.6
	2030	5.4	6.9	29.2	33.7	3.0	78.2
	2040	3.6	7.0	27.6	37.4	3.0	78.5
	2050	2.5	6.5	21.4	35.6	3.0	68.9
	2060	2.0	5.6	15.3	29.9	3.0	55.8
	2070	2.0	4.6	10.7	24	3.0	44.3
	2080	2.1	3.9	7.7	19.5	3.0	36.1
	2090	2.3	3.0	5.8	15.7	3.0	29.8
2100	2.6	2.5	4.2	12.6	3.0	24.9	
B2	1990	22.7	17.9	11.9 + 6.0 = 17.9	4.8 + 6.3 = 11.1	3.0	72.6
	2000	18.6	11.4	15.3 + 8.1 = 23.4	5.3 + 7.3 = 12.6	3.0	69.0
	2010	13.4	9.5	18.6 + 10.7 = 29.3	5.7 + 7.3 = 13.0	3.0	68.2
	2020	8.1	5.8	21.7 + 12.0 = 33.7	7.3 + 7.2 = 14.5	3.0	65.0
	2030	3.9	2.4	21.6 + 13.9 = 35.5	7.1 + 8.0 = 15.1	3.0	59.9
	2040	3.4	0.7	19.5 + 15.8 = 35.3	6.8 + 9.6 = 16.4	3.0	58.8
	2050	3.0	0.6	17.5 + 15.7 = 33.2	6.4 + 11.0 = 17.4	3.0	57.2
	2060	2.6	2.4	10.9 + 15.9 = 26.8	6.5 + 12.4 = 18.9	3.0	53.7
	2070	2.7	2.5	7.8 + 16.4 = 24.2	6.0 + 13.6 = 19.6	3.0	51.9
	2080	2.9	2.8	5.7 + 15.7 = 21.4	5.2 + 13.8 = 19.0	3.0	49.1
	2090	3.2	3.3	5.2 + 15.0 = 20.2	4.4 + 14.1 = 18.5	3.0	48.0
2100	3.6	3.7	4.9 + 14.8 = 19.7	3.4 + 13.8 = 17.2	3.0	47.3	
A2	1990	22.7	17.9	11.9 + 6.0 = 17.9	4.8 + 6.3 = 11.1	3.0	72.6
	2000	18.6	11.4	15.3 + 8.1 = 23.4	5.3 + 7.3 = 12.6	3.0	69.0
	2010	9.4	11.5	18.4 + 16.0 = 34.4	8.2 + 8.1 = 16.3	3.0	74.7
	2020	9.9	12.3	21.6 + 28.3 = 49.9	11.7 + 12.6 = 24.3	3.0	99.5
	2030	10.4	12.3	20.2 + 34.7 = 54.9	12.9 + 18.4 = 31.3	3.0	111.9
	2040	10.5	11.3	17.5 + 33.8 = 51.3	11.2 + 20.9 = 32.1	3.0	108.1
	2050	10.6	10.5	15.1 + 32.9 = 48.0	9.7 + 23.7 = 33.4	3.0	105.4
	2060	9.8	8.1	13.0 + 24.6 = 37.6	6.3 + 21.5 = 27.8	3.0	86.3
	2070	9.2	6.1	11.2 + 18.4 = 29.6	4.1 + 19.7 = 23.8	3.0	71.7
	2080	9.5	4.9	9.8 + 15.3 = 25.1	3.2 + 18.7 = 21.9	3.0	64.2
	2090	10.6	4.0	8.6 + 14.1 = 22.7	2.9 + 18.7 = 21.6	3.0	61.9
2100	11.8	3.2	7.5 + 13.0 = 20.5	2.7 + 19.1 = 21.8	3.0	60.3	
A1FI	1990	22.7	<i>17.0</i>	<i>17.7</i>	<i>10.5</i>	3.0	<i>70.9</i>
	2000	17.0	11.0	25.3	12.8	3.0	69.0
	2010	13.9	10.3	38.8	14.9	3.0	80.8
	2020	4.7	10.5	52.7	16.1	3.0	86.9
	2030	4.0	13.3	57.1	18.6	3.0	96.1
	2040	4.2	13.4	51.9	21.5	3.0	94.0
	2050	5.1	10.7	37.0	24.7	3.0	80.5
	2060	5.2	5.8	24.3	17.9	3.0	56.3
	2070	5.7	3.1	17.0	13.8	3.0	42.6
	2080	6.5	2.4	15.1	12.4	3.0	39.4
	2090	7.3	2.5	14.6	12.4	3.0	39.8
2100	8.0	2.6	14.1	12.4	3.0	40.1	

OECD90, OECD group developed countries; FSU/EE, Former Soviet Union and Eastern Europe, CPA Centrally Planned Asia; Lat Am Latin America; Afr/Mid E Africa and Middle East. The full definitions of the world regions are given on pages 332–333 of Nakicenovic et al. (2000). Note that the emissions actually used at

1990 in the HadCM3 experiments B1 and A1FI were identical to those in B2 and A2 for simplicity in conducting the experiments, rather than the slightly different values tabulated (*italicized*) which reflect revisions between the preliminary and final versions of the respective emissions scenarios

of the geographical characteristics of the emissions scenario, therefore. It is also relevant that there is less wet deposition in the subtropics. There is also a slow accumulation of sulfate in the stratosphere in the model, but separate HadAM3 experiments with emissions fields for various epochs (but present-day SSTs and GHG concentrations) have shown that this is only a minor contributory factor. It should be noted here that variations of oxidant concentrations in response to climate change would be expected to modulate the burden/emissions ratio as well, but we do not model this effect.

In B2 the direct forcing remains fairly constant between 2000 and 2100 (Fig. 5b) like the burden, but the indirect forcing reduces significantly. To a good approximation the direct forcing scales linearly with the global sulfate burden, but this is clearly not the case for the indirect effect. The normalized indirect forcing (i.e. forcing per unit sulfate burden; Fig. 5d) weakens by a large factor (more than a factor of 4 between 1860 and 2100 in B2) as the sulfate burden increases. This is expected partly because the sensitivity of cloud to adding further sulfate at a given location decreases with increasing aerosol. In our formulation of the effect, given that any points where the albedo perturbation would give rise to a cloud albedo greater than unity have their albedos limited, one would also expect this to compound the drop-off of the normalized indirect forcing at high aerosol concentrations, e.g. at 2050 in A2. The difference in normalized indirect forcing between 2000 and 2050/2100 in B2 (despite similar global sulfate burdens) is probably mainly due to the main areas of pollution moving to lower latitudes where layer cloud is less abundant.

It may seem a little surprising at first sight that the fossil-fuel-intensive scenario A1FI gives rise to a lower sulfate burden at 2050 than A2, with consequently weaker aerosol forcing. Indeed, at 2100 the A1FI aerosol burden is lower even than in the B2 case. However, A1FI is an amalgamation of the A1C and A1G scenarios (Nakicenovic et al. 2000). Of these, A1C assumes heavy use of coal, but burned using 'clean' technologies that reduce sulfur emissions; while A1G assumes heavy use of oil and gas, fuels which contain less sulfur.

5.4 Net radiative forcing

Our simulations do not take changes in black carbon and organic carbon into account. Their combined change in radiative forcing tends to cancel in the global average, although this is unlikely to be the case locally. The net global mean forcing from 2000 to 2100 from black carbon and organic carbon combined has been estimated to be about -0.20 W/m^2 in A2 and A1FI (Ramaswamy et al. 2001). The sum of the change in forcings from 2000 to 2100 (excluding the indirect effect of sulfate aerosols) in the model is close to the sum of the anthropogenic components given in Houghton et al. (2001), Appendix II. This is because there is an

additional model contribution from the recovery of stratospheric ozone (Appendix B) which compensates for the shortfall in the contribution from tropospheric ozone and our neglect of black and organic carbon.

The future rate of increase in net radiative forcing in the GB2 scenario is similar to that over recent decades (Fig. 6), and reaches about 4.5 W/m^2 by 2100. In other words, WMGHG forcing in B2 continues the recent trend. If only WMGHGs are included in the forcing (GB2 compared to B2), the net radiative forcing is about 1.0 W/m^2 higher in 1990, and 1.3 W/m^2 higher in 2000 as the negative forcing from stratospheric ozone depletion peaks (Table 3a), but B2 and GB2 then converge again at the end of the twenty first century (Fig. 6). This follows partly from the gradual decrease in sulfur emissions and consequent weakening of that forcing in B2 in the second half of the century (Table 2, Fig. 5b), and partly from the increasing contribution to the anthropogenic forcing from ozone in all SRES scenarios, including B2 (Table 3b).

The forcings in A1FI and A2 diverge sharply from B2 in the 2020s and 2040s respectively (Fig. 6), following the rapid increase in the CO_2 and other GHG emissions relative to B2 at those times (Table 1), while B1 diverges gradually from B2 throughout the twenty first century. Initially, the forcing increases much faster in A1FI because GHG emissions increase faster, and sulfur emissions are lower. Towards the end of the twenty first century, however, this trend is reversed—sulfur and CO_2 emissions rates are then similar in both scenarios, but the emission rates of some trace gases (e.g. CH_4 , HFC-134a) become much higher in A2 (inferred from Table 1). By 2100, the net heating relative to preindustrial values reaches 7.0 and 7.8 W/m^2 in A2 and A1FI respectively (Table 3b), compared to 6.7 W/m^2 in the old G92 (WMGHGs-only) scenario.

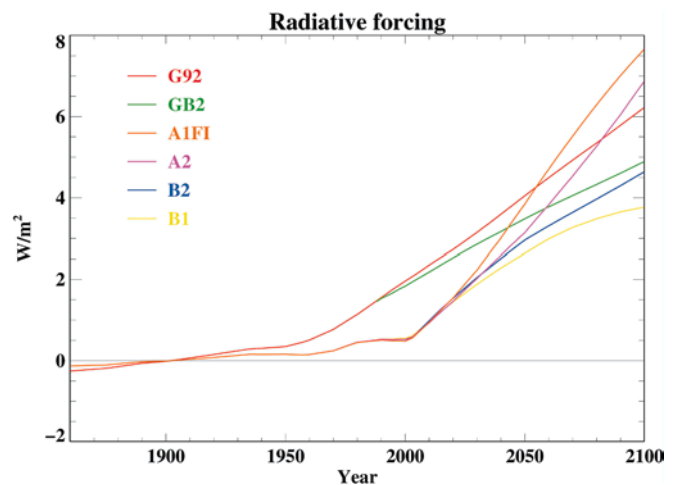


Fig. 6 Time series of annual global mean total forcing at the tropopause computed for the HadCM3 experiments G92, GB2, A1FI, A2, B2 and B1 over the period 1859–2100, each relative to their average over the period 1880–1920. Effects of greenhouse gases, direct and indirect sulfate aerosol forcing, tropospheric and stratospheric ozone changes are included

Table 3a Comparison of HadCM3 global mean present day (2000) forcing relative to pre-industrial values with IPCC 2001 (Ramaswamy et al. 2001) estimated ranges for present-day. The IPCC WMGHG forcings are the quoted central estimates, which have an uncertainty of 10%. HadCM3 figures are from the B2 experiment. The ozone forcing and its range are as estimated using the interactive method (note that the FDH method gives a substantially lower stratospheric effect, within the IPCC range)

Present forcings (W/m ²)	WMGHGs (total)	WMGHGs (minor)	Sulfate (direct)	Sulfate (indirect)	Ozone (Tropospheric)	Ozone (Stratospheric)
HadCM3 2000	2.34	0.84	-0.18	-0.91	[0.19, 0.24]	[-0.59, -0.65]
IPCC 2001	2.43	0.97	[-0.2, -0.8]	[-0.3, -1.8]	[0.25, 0.50]	[-0.09, -0.25]

b HadCM3 global mean forcings at 2100 relative to pre-industrial values in the four SRES experiments A1FI, A2, B2 and B1. Ozone estimates are from the interactive method. The stratospheric ozone forcing contributes +0.17 W/m² in all four scenarios (see Appendix B)

Future forcings (W/m ²)	WMGHGs (total)	WMGHGs (minor)	Sulfate (direct)	Sulfate (indirect)	Ozone (total)	Net
A1FI	7.94	1.45	-0.17	-0.61	0.66	7.82
A2	7.47	1.64	-0.24	-0.79	0.60	7.04
B2	5.29	1.10	-0.18	-0.71	0.49	4.89
B1	4.22	0.72	-0.10	-0.50	0.39	4.01

c Comparison of two alternative estimates of present and future ozone forcing in HadCM3 for 2000, 2050 and 2100 calculated using a diagnostic method in the model allowing interactive adjustment of the stratosphere, and the fixed dynamical heating method (FDH)

Ozone Forcing (W/m ²) Interactive/FDH estimates	A1FI	A2	A2	B1
2000	-0.38/+0.24	-0.37/+0.23	-0.41/+0.22	-0.34/+0.21
2050	0.41/0.60	0.29/0.48	0.29/0.42	0.30/0.35
2100	0.66/0.76	0.60/0.63	0.49/0.46	0.39/0.31

The increase in forcing is slowest in the B1 scenario, which assumes small energy demand, improvements in energy efficiency and the development of non-fossil fuel energy sources (Nakicenovic et al. 2000). Even in this case, however, the forcing reaches 4.0 W/m² by 2100 (Table 3b).

6 Climate change response

In much of the analysis in this section we concentrate on 30-year averages, of annual and seasonal mean (DJF and JJA) variables in order to enhance the signal-to-noise ratio. Two future periods, the ‘2040s’ (the 30-year period from December 2029 to November 2059) and the ‘2080s’ (similar but 2069 to 2099) are chosen. Differences are constructed either relative to a 240-year period of CTL parallel to the forced experiments, or relative to a 30-year present-day period, the ‘1980s’ (as before but 1969 to 1999). In order to estimate noise we use the standard deviation of successive 30-year averages from CTL (see Collins et al. 2001 for more detail on the variability in CTL), and estimate significance levels assuming 30-year average signals sampled from the forced experiments are normally distributed about a mean signal level with standard deviation as estimated from CTL, i.e. with no change of variance in response to forced climate changes.

However, we first consider trends of annual mean quantities over the entire simulation period.

6.1 Global warming, sea level, and sea-ice trends

Of the six scenario experiments G92, GB2, A1FI, A2, B2 and B1 the first two (GHGs only) exhibit overall global warming from 1900 to present somewhat above the observed, whereas the latter four (including other anthropogenic forcings) agree much better with the observed change, represented here by an updated version of the blended MOHSST6-UEA SST and surface air temperature dataset (Parker et al. 1994) (Fig. 7a). Note however that the rate of global warming in recent decades is similar in all cases (A1FI, A2, B2 and B1 being identically forced up to 1989). It is plausible that the inclusion of all anthropogenic forcings in the A1FI, A2, B2 and B1 cases is more realistic in representing the twentieth century record, but it is not our purpose to deal with detailed attribution analysis using these simulations—that question is addressed by Tett et al. (2002). For the sake of discussion of the future forced responses we simply assume that the results are a reasonable guide to the future given the scenario inputs, but a number of caveats are also discussed later.

Relative to 1900, simulated global warming spans a range of about 1.5 to 2.5 K at 2050 rising to 2.6 to 5.3 K in 2100. The upper envelope is defined by G92 and GB2 up to about 2050, but A1FI warms most thereafter, while the lower envelope is provided by A2 up to about 2030 and thereafter by B1. The A2 and A1FI warmings rise particularly steeply in the mid twenty first century, following the increase of emissions discussed in Sect. 5. Over

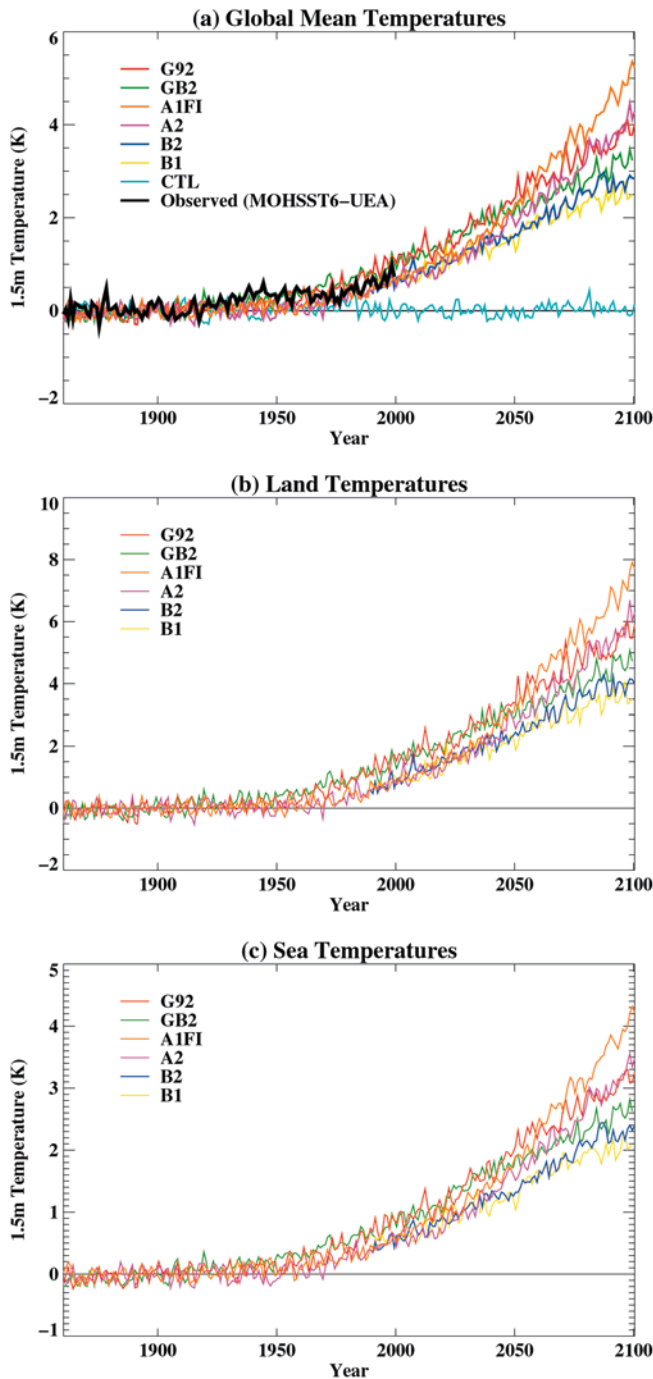


Fig. 7 **a** Time series of annual global mean temperatures in G92, GB2, A1FI, A2, B2, B1 and CTL for the period 1859–2100, each relative to their average over the period 1880–1920. Observed global mean temperature anomalies from the MOHSST6-UEA dataset (Parker et al. 1994) are also shown. **b, c** Time series of land and sea temperatures as **a** but omitting CTL and observations

the last decade or so of the twenty first century A1FI is warmer than the other scenarios by a clear 1 K or more (Fig. 7a). The global mean temperature response essentially tracks the graph of estimated global mean forcing through time in the six experiments (Fig. 6), with a warming at 2100 of about 0.55–0.65 K/[W/m²].

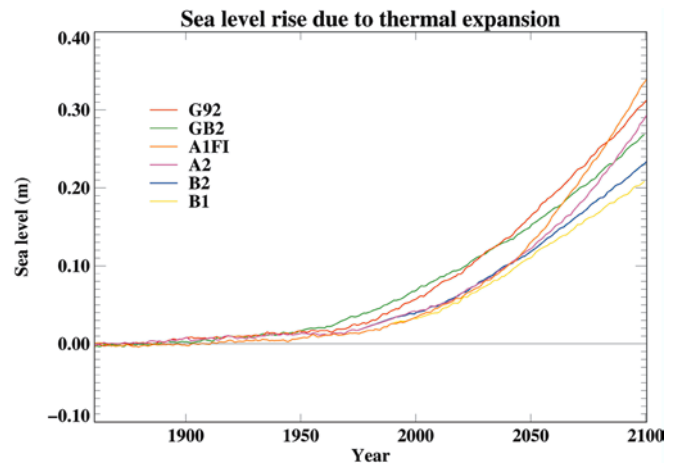


Fig. 8 Time series of annual global mean sea level rise due to thermal expansion in G92, GB2, A1FI, A2, B2 and B1 relative to CTL

Land and sea temperatures (Fig. 7b, c) mirror the rise in global means but with a fairly consistent land–sea contrast in the transient response with a land/sea ratio of about 1.7; higher than in some other models (e.g. EC-HAM4-OPYC; Roeckner et al. 1999, hereinafter referred to as R99), but similar to that in HadCM2 (Mitchell et al. 1999).

Sea level rise is an important consequence of climate change, leading to both the relatively slow inundation of low-lying coastal areas and an increase in the frequency of short-lived extreme high water events. The largest contribution to the predicted rise in future global-mean sea level during the period 1900 to 2100 is from the thermal expansion of the ocean, calculated from the changes in temperature structure of the model ocean (Gregory and Lowe 2000). Relative to 1900, the predicted thermal expansion ranges between about 21 to 34 cm (Fig. 8), again smallest for B1 and largest for A1FI. The rate of sea level rise is particularly steep for A1FI and A2 after 2050. When a (provisional) estimate of the contribution to sea level rise from the melting of land ice is also included (Gregory and Lowe 2000), the total increase in mean sea level ranges from 30 to 48 cm. Because of the long time scales associated with sea level rise, even if the concentrations of atmospheric CO₂ were stabilized at 2100, the sea level would continue to rise for at least several centuries.

While sea level is predicted to rise almost everywhere, there is considerable spatial variation. In some regions, the rise is slightly negative or close to zero, in others up to twice the global mean. The predicted patterns of sea level rise (not shown) exhibit the largest increases in parts of the north Pacific and to the west of Greenland. For A2 (an intermediate member of the six scenarios considered here), the maximum rise is 75 cm, occurring in the northwestern Pacific near Japan. However, Gregory et al. (2001) recently compared the patterns of sea level rise predicted by different climate models for the same emissions scenario and found many of the

regional details to be model-specific. Thus, our confidence in the predicted spatial patterns of sea level rise is currently less than for temperature change patterns.

Melting of sea ice in response to global warming becomes apparent in the second half of the twentieth century (Fig. 9), at least in G92 and GB2 which produce quite marked thinning of Arctic ice. The decline in Arctic ice in B2 over this period is less pronounced, though it starts to accelerate late in the century. Both area and volume of Arctic ice continue to decline strongly in all six cases throughout the twenty first century, the relatively more rapid decrease in volume indicating that the remaining ice continues to thin. By 2100 the annual mean areal coverage in the Arctic falls to between about 40% (A1FI), 50% (A2,G92), 60% (B2, GB2) and 65% (B1) of that in CTL, and the annual mean volume to between about 22% (A1FI) and 50% (B1). A steady decrease also occurs in Antarctic sea ice, but to a lesser extent than in the Arctic and with relatively less variation between the six experiments.

6.2 Trends in the hydrological cycle and energy balance

Global-mean annual precipitation (see Tables 4a, b) is enhanced in the warmer climate, with a sensitivity around 1%/K (about 1.4%/K in the GHG-only scenarios). The cloud feedbacks are almost neutral, at least in the GHG-only cases G92 and GB2, as shown by the small change in net cloud forcing in the 2040s and 2080s (Tables 4a, b). (This diagnostic cannot be used to determine the cloud feedback in the A1FI, A2, B2 and B1 experiments as it is affected by an increase in upward solar flux and small decrease in LW flux due to the sulfate aerosols). There is enhanced radiative cooling of the atmosphere in all the experiments (balanced mainly by increased latent heat of condensation) and increased radiative heating of the surface (mainly due to reduced longwave cooling) which is balanced by increased evaporation (Tables 4a, b). Over the sea, increased radiative heating at the surface is balanced mainly by enhanced evaporative cooling, whereas over land, the dominant term maintaining the balance is enhanced sensible heat (Table 4c). This arises because evaporation

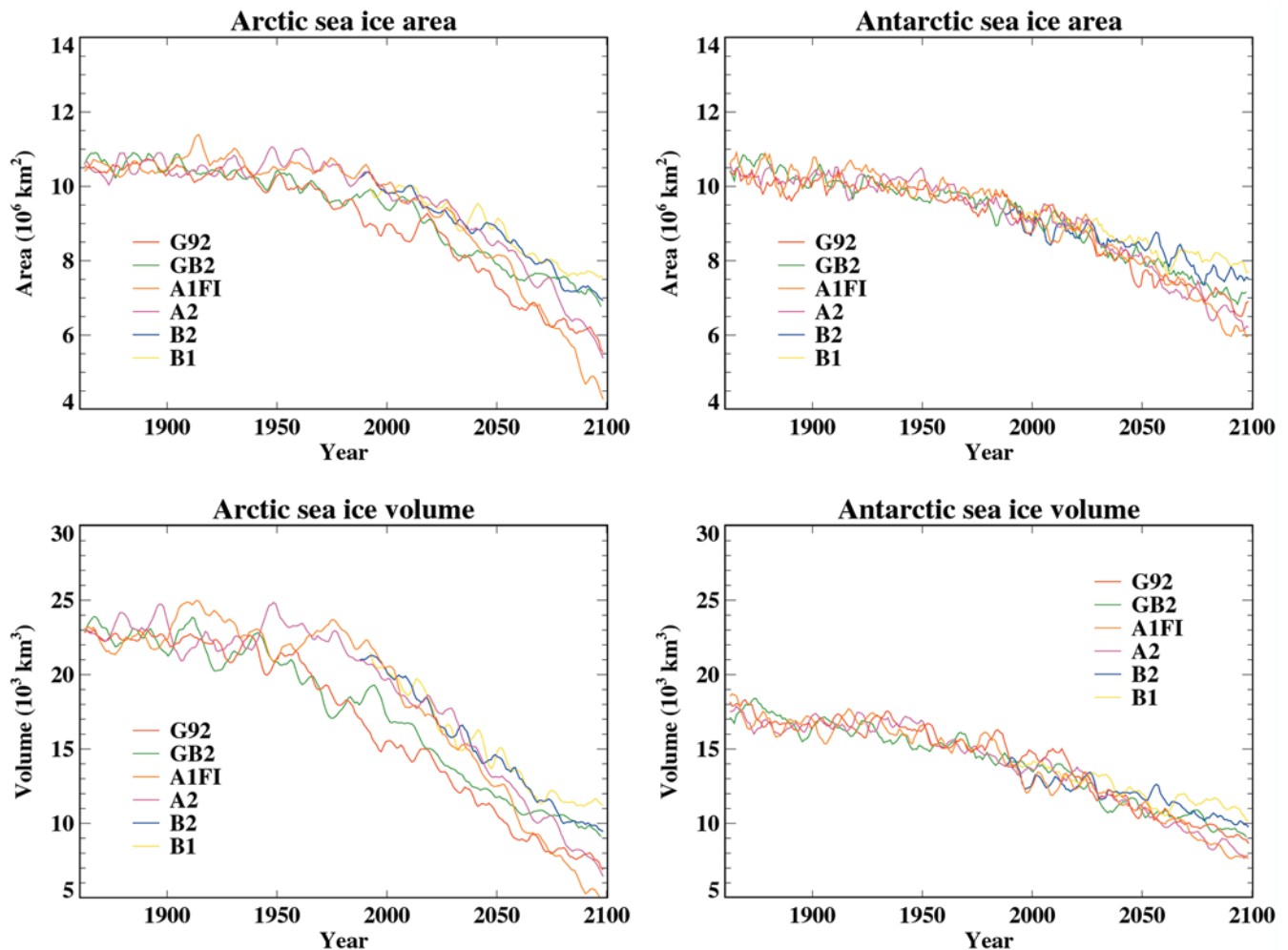


Fig. 9 Time series of annual mean total sea ice areal coverage and volume in the Arctic and Antarctic in G92, GB2, A1FI, A2, B2 and B1; smoothed using a 5-year running mean

Table 4a Global mean radiative, energy and water fluxes in the control run (CTL) and the corresponding differences in the forced experiments relative to the control run for the 2040s period

Global means	CTL	G92	GB2	B1	B2	A2	A1FI
Atmospheric fluxes (2040s)	(W/m ²)						
SW at TOA (net)	240.42	1.86	1.79	0.30	0.55	0.40	0.67
LW at TOA (up net)	-240.59	-0.62	-0.75	0.63	0.47	0.80	0.70
LW at TOA (up – CS)	-262.16	-0.22	-0.36	1.16	1.03	1.45	1.34
LW at TROP (net)	-225.47	-0.92	-0.72	0.58	0.36	0.73	0.61
Net radiation at TOA	-0.17	1.24	1.03	0.93	1.02	1.19	1.37
Net radiation at TROP	1.86	1.12	0.95	0.87	0.92	1.10	1.26
SW cloud forcing	-49.65	0.37	0.35	-0.30	-0.24	-0.25	-0.23
LW cloud forcing	21.57	-0.4	-0.39	-0.53	-0.56	-0.65	-0.64
Net cloud forcing	-28.07	-0.03	-0.04	-0.84	-0.80	-0.90	-0.88
Atmospheric radiative heating	-101.88	-2.49	-2.22	-0.99	-1.26	-1.14	-1.38
Atmospheric greenhouse effect	154.28	11.98	10.51	8.55	9.06	10.25	11.18
Hydrological fluxes (2040s)	(mm/day)						
Total precipitation	2.903	0.091	0.083	0.039	0.051	0.047	0.055
Dynamic precipitation	0.723	0.021	0.020	0.010	0.013	0.015	0.017
Convective precipitation	2.180	0.069	0.062	0.029	0.038	0.032	0.038
Evaporation + sublimation	2.904	0.091	0.083	0.039	0.051	0.047	0.056
Surface energy (2040s)	(W/m ²)						
SW (net)	164.34	-0.07	-0.24	-1.16	-1.07	-1.39	-1.38
LW (emitted)	-394.87	-12.60	-11.27	-7.92	-8.59	-9.45	-10.48
Surface net radiation	101.71	3.72	3.25	1.91	2.28	2.33	2.75
Sensible heat	-16.98	0.01	0.07	0.06	0.12	0.12	0.10
Latent heat	-84.15	-2.62	-2.39	-1.12	-1.46	-1.35	-1.60
Surface net heat flux	0.57	1.12	0.93	0.85	0.94	1.09	1.25
SAT at 1.5 m (2040s) (K)	286.65	2.43	2.17	1.54	1.66	1.83	2.03

Positive fluxes indicate a net downwards flux or into the layer considered. (TOA, top of atmosphere; TROP, tropopause; SW, shortwave, LW, longwave; CS, clear-sky, SAT, surface air temperature)

b As Table 4a but global mean differences for the 2080s period

Global means	CTL	G92	GB2	B1	B2	A2	A1FI
Atmospheric fluxes (2080s)	(W/m ²)						
SW at TOA (net)	240.42	2.58	2.31	1.44	1.52	1.98	2.81
LW at TOA (up net)	-240.59	-1.00	-1.05	-0.47	-0.28	-0.08	-0.58
LW at TOA (up – CS)	-262.16	-0.66	-0.75	-0.01	0.24	0.62	0.05
LW at TROP (net)	-225.47	-1.28	-0.99	-0.26	-0.08	0.14	-0.39
Net radiation at TOA	-0.17	1.58	1.26	0.97	1.24	1.91	2.23
Net radiation at TROP	1.86	1.41	1.14	0.87	1.11	1.72	2.00
SW cloud forcing	-49.65	0.41	0.36	-0.00	-0.02	0.01	0.29
LW cloud forcing	21.57	-0.34	-0.29	-0.46	-0.52	-0.70	-0.62
Net cloud forcing	-28.07	0.07	0.07	-0.47	-0.54	-0.69	-0.33
Atmos. Radiative heating	-101.88	-3.57	-2.92	-2.11	-2.22	-2.66	-3.34
Atmos. Greenhouse effect	154.28	18.32	14.90	11.95	13.81	18.61	21.96
Hydrological fluxes (2080s)	(mm/day)						
Total precipitation	2.903	0.123	0.099	0.076	0.077	0.094	0.112
Dynamic precipitation	0.723	0.029	0.025	0.018	0.020	0.025	0.026
Convective precipitation	2.180	0.094	0.075	0.058	0.057	0.069	0.085
Evaporation + sublimation	2.904	0.124	0.100	0.076	0.077	0.095	0.113
Surface energy (2080s)	(W/m ²)						
SW (net)	164.34	-0.69	-0.64	-1.07	-1.38	-1.85	-1.81
LW (emitted)	-394.87	-19.32	-15.94	-12.43	-14.10	-18.69	-22.53
Surface net radiation	101.71	5.15	4.18	3.08	3.45	4.57	5.58
Sensible heat	-16.98	-0.19	-0.19	-0.02	-0.13	-0.12	-0.32
Latent heat	-84.15	-3.55	-2.87	-2.20	-2.22	-2.71	-3.23
Surface net heat flux	0.57	1.41	1.12	0.86	1.11	1.74	2.02
SAT at 1.5 m (2080s) (K)	286.65	3.67	3.04	2.38	2.70	3.56	4.26

is restricted over parts of the continents, and the surface temperature is generally higher over the ocean than over well-watered land, making evaporation a more efficient means of losing energy than sensible heat. There is an

increase in the flux of moisture from ocean to land in all experiments.

The global sensitivity of precipitation for a given warming is much higher than in ECHAM4-OPYC

c As Table 4b, but differences for land and sea points meaned separately for the 2080s period

Land and sea means	CTL	G92	GB2	B1	B2	A2	A1FI
Atmospheric fluxes (Land)	(W/m ²)						
SW at TOA (net)	214.53	6.60	5.92	3.69	4.23	5.43	7.14
LW at TOA (up net)	-233.94	-4.10	-3.74	-2.49	-2.66	-3.05	-4.26
LW at TOA (up - CS)	-251.54	-4.02	-3.62	-2.15	-2.22	-2.63	-3.95
LW at TROP (net)	-217.94	-4.55	-3.82	-2.35	-2.56	-2.97	-4.28
Net radiation at TOA	-19.41	2.50	2.19	1.20	1.58	2.38	2.88
Net radiation at TROP	-16.45	2.19	1.98	1.04	1.36	2.09	2.48
SW cloud forcing	-34.60	3.69	3.37	1.87	2.33	2.90	3.76
LW cloud forcing	17.60	-0.08	-0.12	-0.34	-0.43	-0.42	-0.31
Net cloud forcing	-17.00	3.61	3.26	1.53	1.90	2.48	3.45
Atmospheric radiative heating	-90.63	-2.07	-1.56	-1.21	-1.17	-1.24	-1.60
Atmospheric greenhouse effect	132.77	24.26	19.66	15.40	17.78	24.44	29.37
Atmospheric fluxes (Sea)	(W/m ²)						
SW at TOA (net)	250.97	0.94	0.83	0.53	0.41	0.58	1.05
LW at TOA (up net)	-243.30	0.27	0.05	0.35	0.69	1.14	0.93
LW at TOA (up - CS)	-266.49	0.72	0.41	0.86	1.24	1.94	1.67
LW at TROP (net)	-228.54	0.05	0.16	0.59	0.93	1.41	1.20
Net radiation at TOA	7.67	1.21	0.89	0.87	1.10	1.71	1.97
Net radiation at TROP	9.33	1.09	0.80	0.81	1.01	1.57	1.80
SW cloud forcing	-55.78	-0.93	-0.87	-0.77	-0.98	-1.17	-1.13
LW cloud forcing	23.19	-0.45	-0.36	-0.51	-0.56	-0.81	-0.75
Net cloud forcing	-32.59	-1.38	-1.23	-1.28	-1.54	-1.98	-1.87
Atmospheric radiative heating	-106.47	-4.18	-3.47	-2.48	-2.65	-3.24	-4.05
Atmospheric greenhouse effect	163.04	15.90	12.96	10.55	12.20	16.24	18.94
Hydrological fluxes (Land)	(mm/day)						
Total precipitation	2.126	0.060	0.021	-0.004	-0.017	0.013	0.014
Dynamic precipitation	0.567	0.018	0.016	0.008	0.011	0.014	0.014
Convective precipitation	1.559	0.042	0.005	-0.012	-0.029	-0.001	0.000
Evaporation + sublimation	1.413	-0.072	-0.068	-0.059	-0.080	-0.105	-0.134
Hydrological fluxes (Sea)	(mm/day)						
Total precipitation	3.219	0.149	0.131	0.109	0.115	0.127	0.151
Dynamic precipitation	0.786	0.033	0.028	0.023	0.024	0.030	0.031
Convective precipitation	2.433	0.116	0.103	0.086	0.092	0.097	0.120
Evaporation + sublimation	3.512	0.203	0.168	0.132	0.141	0.176	0.213
Surface energy (Land)	(W/m ²)						
SW (net)	139.75	3.90	3.58	1.64	1.87	2.31	3.32
LW (emitted)	-366.71	-28.37	-23.39	-17.89	-20.44	-27.49	-33.63
Surface net radiation	71.22	4.57	3.75	2.41	2.75	3.62	4.47
Sensible heat	-29.46	-6.66	-5.74	-4.14	-5.05	-6.66	-8.35
Latent heat	-41.08	2.12	2.00	1.74	2.33	3.09	3.93
Surface net heat flux	0.68	0.02	0.01	0.01	0.02	0.05	0.05
Surface Energy (Sea)	(W/m ²)						
SW (net)	174.36	-2.56	-2.35	-2.17	-2.70	-3.55	-3.90
LW (emitted)	-406.35	-15.64	-12.90	-10.20	-11.51	-15.10	-18.01
Surface net radiation	114.13	5.39	4.36	3.35	3.74	4.95	6.02
Sensible heat	-11.90	2.45	2.06	1.66	1.88	2.55	2.95
Latent heat	-101.70	-5.86	-4.85	-3.80	-4.07	-5.08	-6.15
Surface net heat flux	0.53	1.98	1.57	1.21	1.55	2.43	2.82
SAT at 1.5 m (Land) (K)	280.29	5.27	4.38	3.37	3.83	5.10	6.20
SAT at 1.5 m (Sea) (K)	289.24	3.02	2.49	1.98	2.24	2.93	3.47

(R99). The reasons for the difference are not entirely clear, especially as only the G92 and R99 GHG experiments are directly comparable. On examining the changes in these two experiments for the 2040s when the global mean warmings in G92 and GHG are 2.43 K and 2.39 K respectively (Table 5), one finds that the increase in the net downward flux at the top of the atmosphere is similar in both experiments, but that there is a greater increase in the radiative heating of the surface in G92 (3.7 cf. 2.2 W/m²), and more negative warming (more cooling) in the atmosphere (-2.5 cf. -0.8 W/m²) (Table 5). Thus, in G92 the surface is being warmed

and atmosphere cooled relative to GHG. This is balanced by greater surface evaporation and atmospheric condensation (precipitation) in G92.

Boer (1993) argued that the increase in precipitation in a version of the Canadian Climate Centre model per degree of global warming was less than in other models at the time because of a negative shortwave cloud feedback, predominantly in the tropics, limiting the total energy imbalance and hence the change in latent heat flux required to maintain surface energy balance.

The shortwave cloud feedback is negative in GHG (R99), as in the Boer (1993) picture, but weakly positive

Table 5 Comparison of the climate response in the 2040s period for the HadCM3 G92 experiment against the similar scenario experiment GHG(R99) conducted with the ECHAM4-OPYC model (Roeckner et al. 1999)

Changes from control (2040s)	G92	GHG(R99)
Surface temperature (K)	2.46	2.39
Precipitation (%)	3.1	1.62
Net TOA heating (W/m^2)	1.2	1.4
Solar cloud forcing (W/m^2)	0.4	-1.4
Surface sensible heat (W/m^2)	0.0	0.7
Surface latent heat (W/m^2)	-2.6	-1.4
Surface radiative heating (W/m^2)	3.7	2.2
Atmospheric radiative heating (W/m^2)	-2.5	-0.8

in G92 (the resultant of a positive feedback over land and negative feedback over sea; Table 4a, c). This contributes to the relatively smaller increase in surface heating in GHG compared to G92. The differences between GHG and G92 in their radiative cooling response in the atmosphere are most likely due to differences in their changes in longwave radiation, though this cannot be inferred directly from the available diagnostics. A smaller increase in longwave cooling of the atmosphere in GHG would be consistent with a smaller increase in precipitation. The main difference in precipitation changes is over the ocean, where precipitation increases by 1.7%/K warming in G92 by the 2040s whereas it decreases in GHG.

Signal to noise ratio is well known to be lower in the precipitation response than for temperature changes. This is most markedly illustrated in the contrast between land and sea precipitation responses (Fig. 10). While a consistent trend signal is clear for sea points, the trends in global-mean land precipitation are extremely variable even after smoothing to filter sub-decadal time scales. Only G92 shows anything resembling a consistent rising trend for global-mean land precipitation; GB2 shows an initial rising trend similar to G92 up to 2050 but then a fall back to near the control run value at 2100. Of note is the fact that A1FI/B1 and A2/B2 show falling trends up to present-day, by contrast with G92 and GB2, since this might provide some discrimination in detection and attribution studies. (However, Allen and Ingram 2002 found that natural forcings dominate anthropogenic forcings in precipitation trend signals over land.) Future trend projections in A1FI, A2, B2 and B1 are quite variable, with little overall change from CTL by 2100.

6.3 Geographical annual-mean and seasonal signals

Although global-mean changes are useful as a summary of the responses to the different emissions scenarios, the geographical distribution of the changes is needed to determine the impact of the different scenarios. Here we list the main features of the geographical patterns of response in temperature, precipitation and soil moisture. The changes are formed by subtracting a long term mean from the control simulation from the ‘2040s’ or

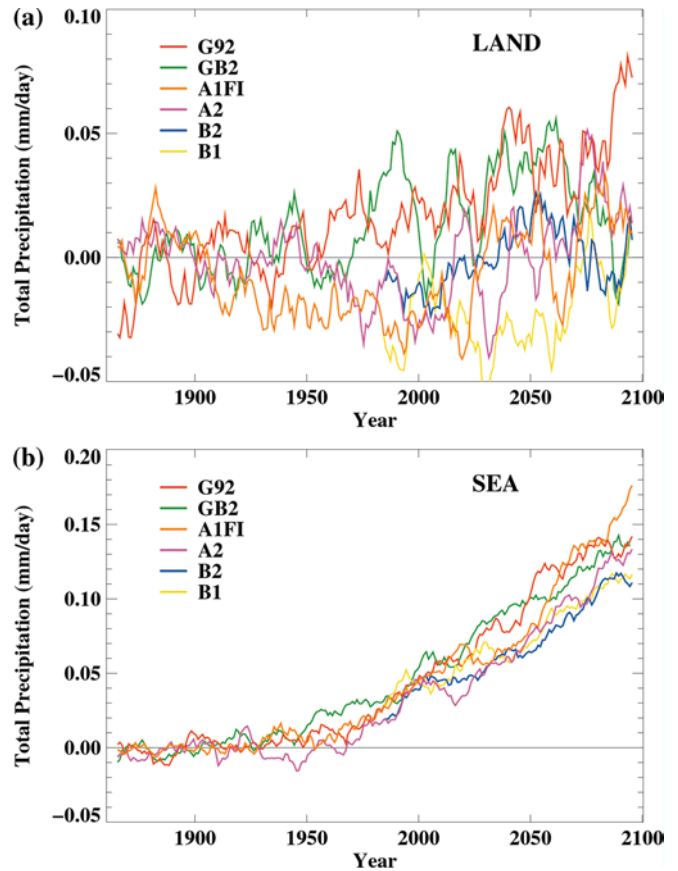


Fig. 10 Time series of annual mean total precipitation over **a** land and **b** ocean in G92, GB2, A1FI, A2, B2 and B1 for the period 1859–2100, each relative to their average over the period 1880–1920; smoothed using an 11-year running mean

‘2080s’ mean for each scenario. We also note the main effects of non-GHG forcings (aerosols plus ozone changes) in the B2 scenario, and the key differences from the patterns obtained using an earlier model, HadCM2 (Mitchell and Johns 1997, hereinafter referred to as MJ97). The large-scale features of the response patterns are remarkably consistent for the alternative scenarios considered. In the next subsections, we consider specific regions and assess statistically the changes in selected parameters.

6.3.1 Annual mean temperature

The patterns of temperature change are similar in the four scenarios A1FI, A2, B2 and B1 (Fig. 11), with a warming everywhere that gets progressively larger in going from B1–B2–A2–A1FI. The patterns are similar to those obtained in other models (e.g. Cubasch et al. 2001), the warming is larger over land than sea, largest in and around the Arctic, and less than the global average over the northern North Atlantic, much of the Southern Ocean and over Southeast Asia. There is a large warming over the Amazon basin which is not always found in other models.

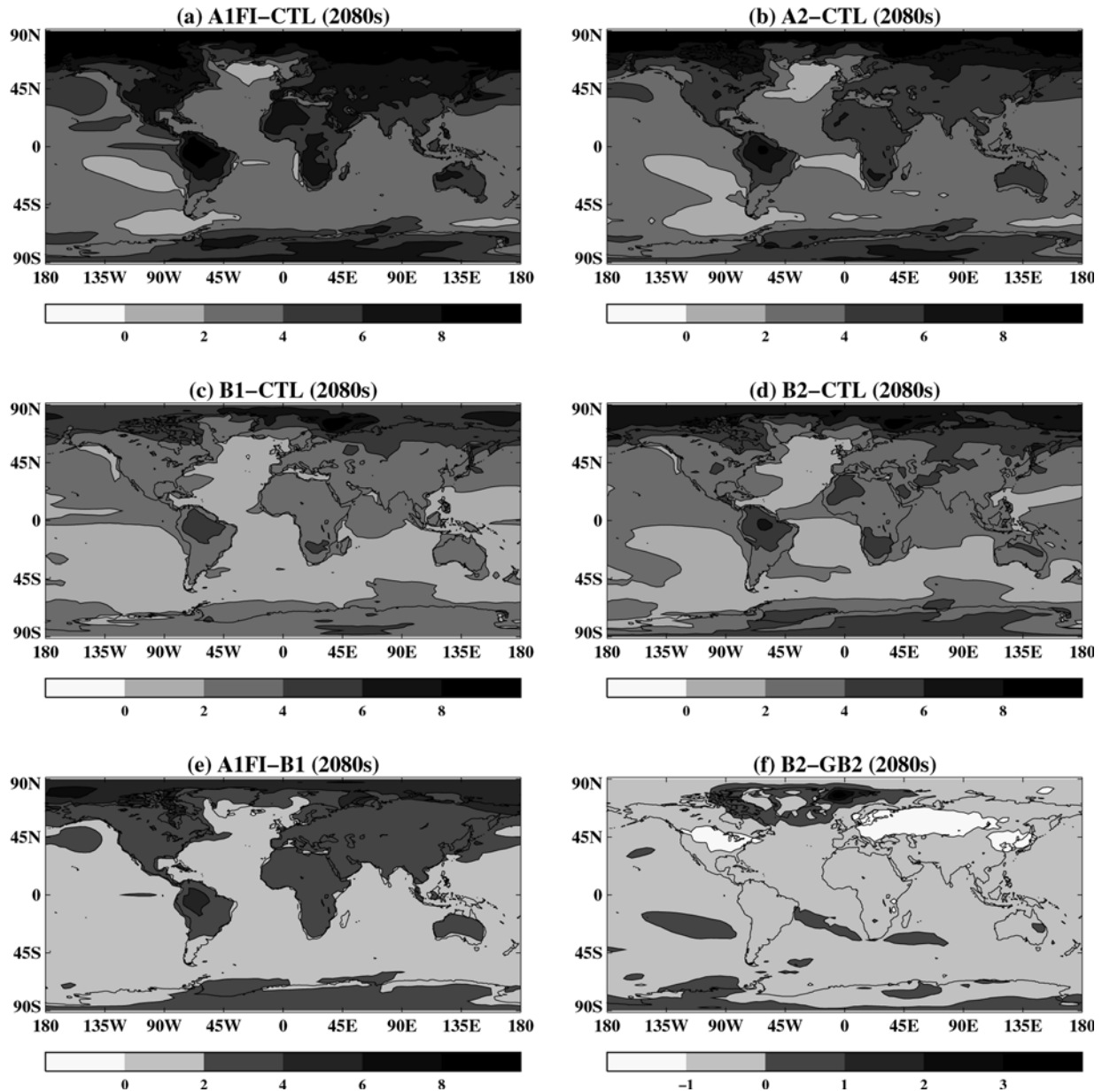


Fig. 11 Annual mean changes in surface air temperature (averaged over years 2070–2099) for **a** A1FI minus control; **b** A2 minus control; **c** B1 minus control; **d** B2 minus control; **e** A1FI minus B1; and **f** B2 minus GB2. Contours every 1 K in **f**, every 2 K otherwise

The effect of adding non-GHG anthropogenic forcings in the B2 scenario is to reduce the warming, especially in the Northern Hemisphere (Fig. 11f). In fact much of the northern continents around 45°N are 1 K or more cooler than in the case with GHGs only. This is largely due to the cooling effect of aerosols, concentrated in the vicinity of these land areas.

There is less warming in the tropics and more in the extra-tropics than in experiments using HadCM2 (see MJ97). In HadCM2, there was a secondary maximum in the warming in the tropics which arose from differences in the treatment of cloud and the boundary layer – see Williams et al. (2001a) for a detailed analysis of the differences in the response of the two models.

6.3.2 Precipitation

As with temperature, the patterns of change in precipitation are similar, with the smallest changes in B1 and the largest in A1FI (Figs. 12, 13). There are increases in the extratropics associated with enhanced poleward transport of moisture arising from the increase in atmospheric humidity (e.g. Manabe and Wetherald 1975) and decreases over much of the subtropics. Precipitation generally increases along the Intertropical Convergence Zone (ITCZ) although there are also some regions of decrease. Over the tropical oceans, there are increases to the north of the equator and decreases to the south. This is symptomatic of a northward shift in the ITCZ

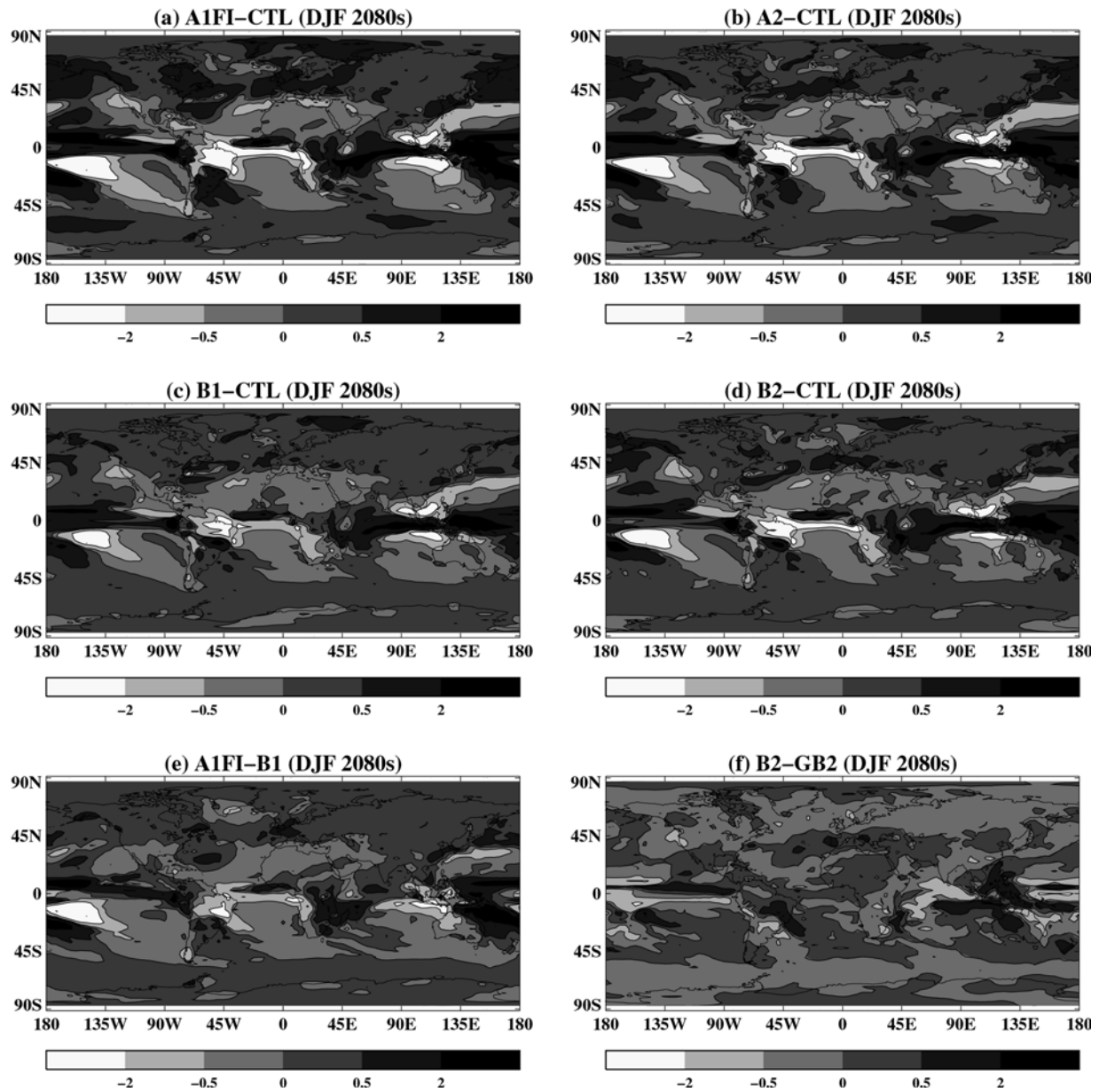


Fig. 12a–f As Fig. 11, but for precipitation changes in December to February. Contours at -2 , -0.5 , 0 , 0.5 and 2 mm/day

associated with the warming being greater in the Northern Hemisphere, and hence displacing the “thermal equator” in that direction. A similar northward shift was noted in an experiment with an older version of the Hadley Centre coupled model (Murphy and Mitchell 1995).

In northern summer, the area of decrease in the subtropics extends further north into the United States, Europe and much of central Asia (Fig. 13). In general, summer precipitation increases (over Southeast Asia and parts of Africa during June to August, and eastern South America, East Africa and Northeast Australia during December to February). The main exception is the northern part of the Amazon Basin, where precipitation decreases throughout the year. The increases in

precipitation in high southern latitudes are more pronounced and extend further north during June to August than December to February.

Adding non-GHG effects in the B2 scenario has only a small effect on precipitation, generally weakening the response (Figs. 12f, 13f). Note particularly the reduced increases over Southeast Asia and smaller reductions over southern Europe during June to August (Fig. 13f). This is similar to the response to aerosols noted by MJ97 using an earlier model in which the effect of aerosols was represented by an increase in surface albedo.

By contrast with MJ97, the precipitation increases are shifts to the north rather than an in situ enhancement. This is consistent with the differences in the change in zonally averaged temperatures. In

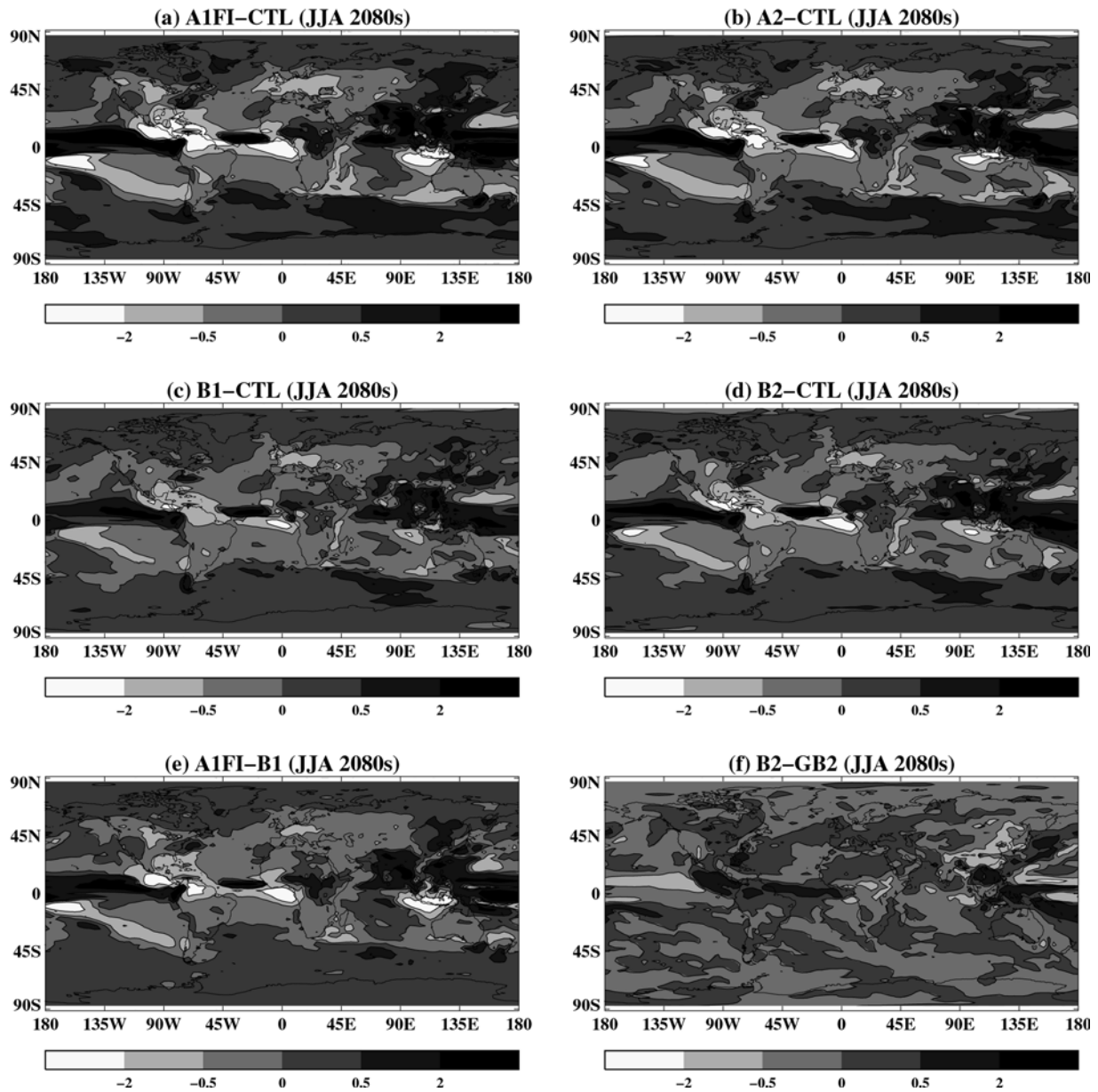


Fig. 13a–f As Fig. 12, but for precipitation changes in June to August

HadCM3, there is greater warming in the Northern Hemisphere leading to a northward shift in the ITCZ; in MJ97, there is a local maximum in the warming at the equator which enhances the ITCZ where it is. A more detailed analysis of the reasons for the difference in response of the two models is given by Williams et al. (2001a). A second major difference is that there are decreases in precipitation during June to August over much of the northern mid-latitude land surface including the United States and Europe, and increases over India (Fig. 13), whereas MJ97 found little change or increases in mid-latitudes, and a drying over much of India at this time of year. Climate impact studies using the two sets of results are likely to come to very different conclusions.

6.3.3 Soil moisture

Once again, the patterns of change are very similar in the A1FI, A2, B2 and B1 scenarios. In the Northern Hemisphere, the changes are much as one would expect from the changes in precipitation; the northern extratropical continents are wetter in winter (Fig. 14), but become drier than in the control climate over much of North America and Europe in summer (Fig. 15). Northern Canada and Siberia are wetter all year, as are regions affected by tropical monsoons, except for the northern part of South America. The changes over Australia vary from scenario to scenario.

The main differences from MJ97 are evident during June to August, when the tropics and subtropics are

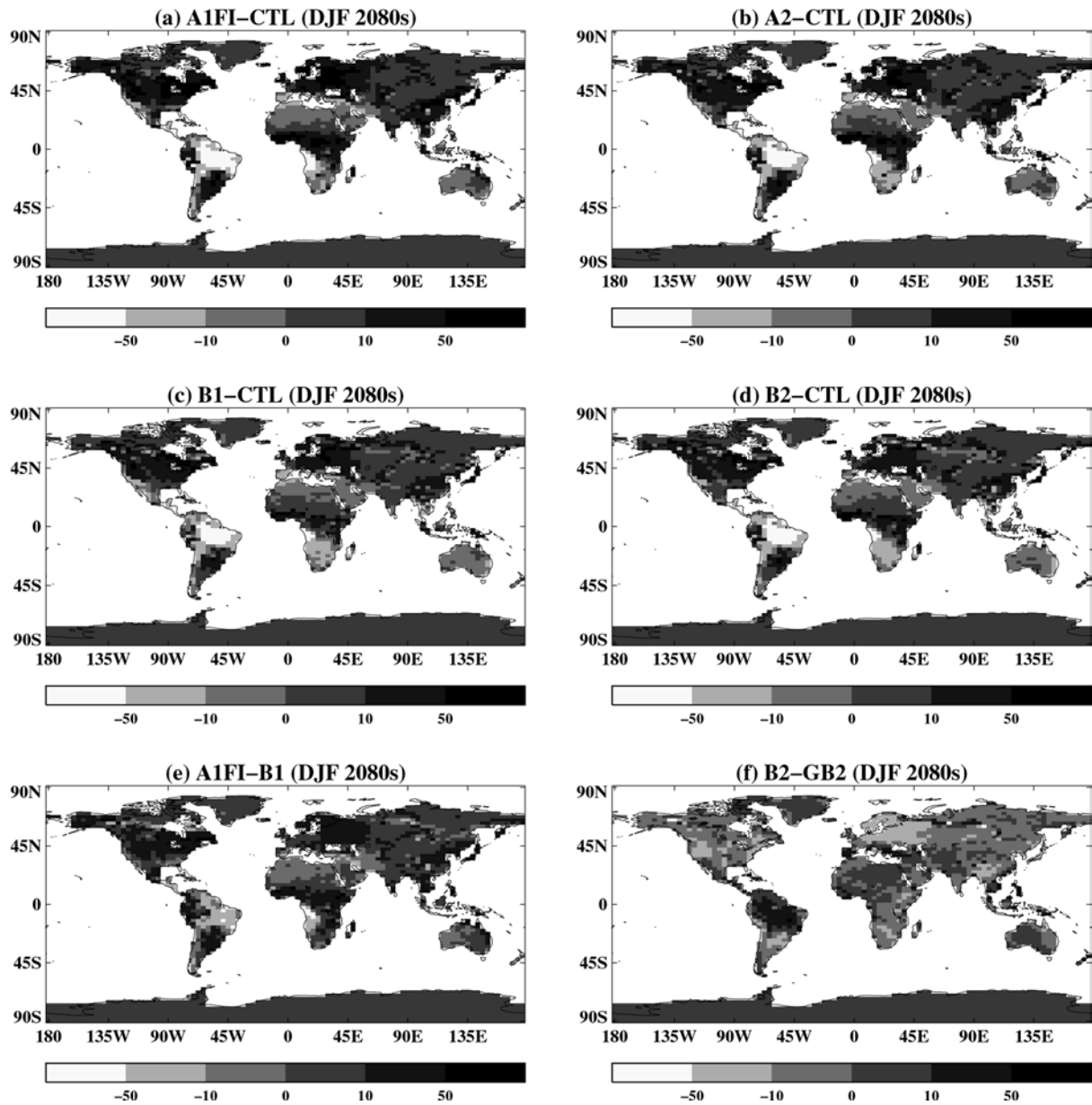


Fig. 14a–f As Fig. 12, but for soil moisture content changes in December to February. Contours at -50 , -10 , 0 , 10 and 50 mm of water equivalent

wetter rather than drier, and Europe is drier rather than wetter. These differences arise partly from the different patterns of temperature response, linked to some extent in Eurasia to sulfate aerosol forcing differences, and partly from the changes made to the land-surface parametrizations (see Williams et al. 2001a).

6.4 Regional signals and their significance

The climate change response of annual-mean temperature, DJF and JJA precipitation in the 2040s and 2080s relative to the 1980s is summarized in Table 6a–c for the globe and five selected land regions defined and assessed previously by IPCC (Houghton et al. 1990, 1996). We do

not consider the fidelity of the control simulation, just the signals of climate change and their significance for these regions.

Not surprisingly, all six scenario experiments give significant warming in annual mean temperatures over all regions in both periods, the highest warming being in the mid-USA (reaching $+4.9$ K in A2 and $+6.6$ K in A1FI in the 2080s), and the lowest in Australia (just $+1.8$ K in B1 in the 2080s). Southern Europe and the Sahel warm slightly less than the mid-USA, but more than Southeast Asia and Australia to maintain a generally north–south gradient in land temperature response, except that the Sahel warms relatively strongly compared to Southern Europe (particularly in the GHG-only experiments in the 2080s).

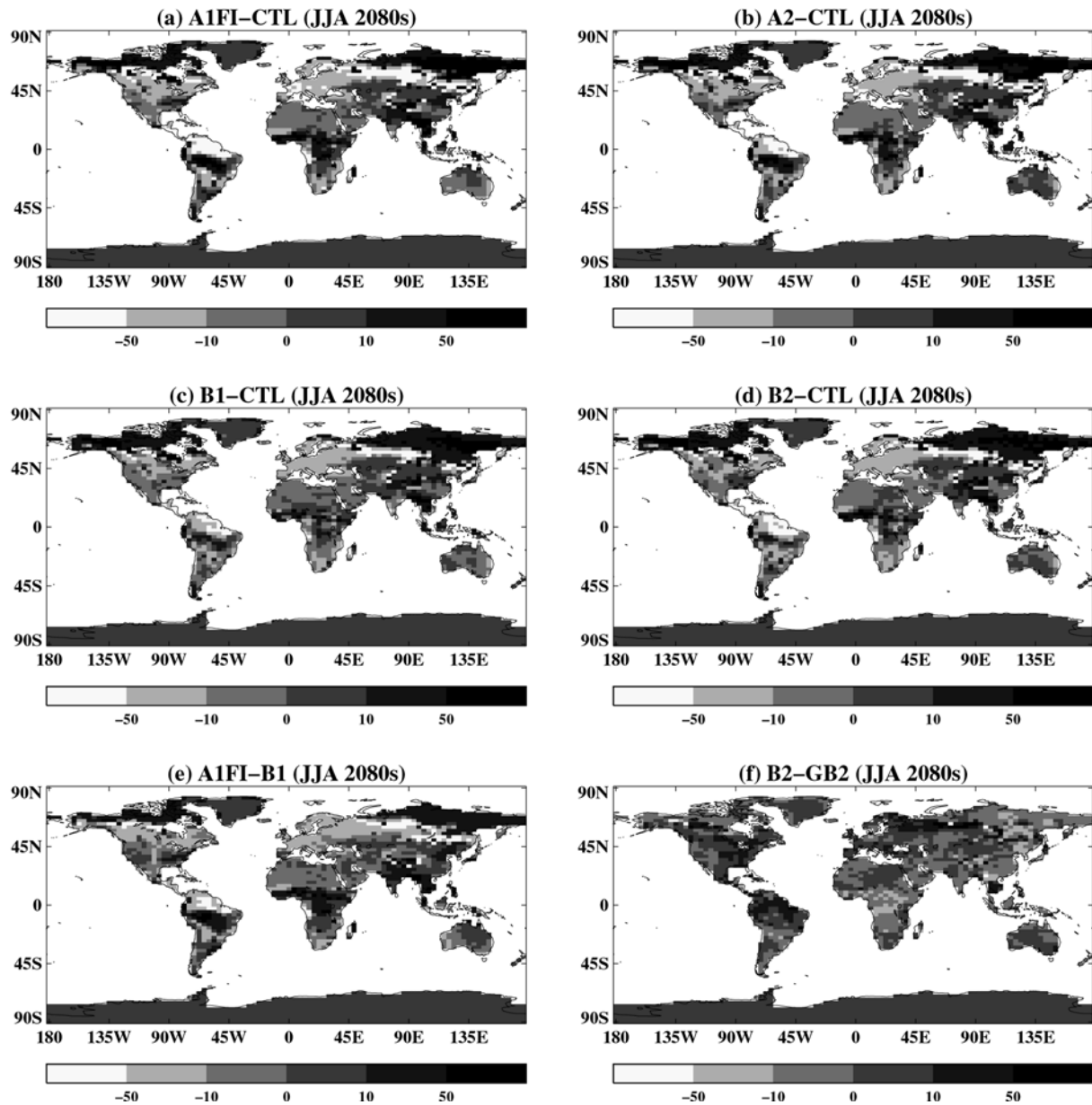


Fig. 15a–f As Fig. 14, but for soil moisture content changes in June to August

Comparison of the response in B2 minus GB2 (i.e. the effect of additional anthropogenic forcings in the B2 scenario) reveals only small differences for these land regions, South east Asia is significantly colder in the 2040s, and Australia significantly colder in the 2080s in B2 relative to GB2; all other differences are insignificant. Globally, B2 is colder than GB2 in the 2040s, but recovers to match GB2 by the 2080s. The relative differences in global mean forcing between the 1980s and 2080s (Fig. 6) might suggest that B2 should show a relatively warmer signal than GB2 in the 2080s due to a reduction in the ozone cooling (sulfate forcing not having changed substantially). But the temperature response to global mean ozone forcing (at least as estimated using the interactive method) is not very linear in

a regional or even global sense, a point that requires more investigation.

Seasonal DJF and JJA precipitation responses (Table 6b, c) in the six scenarios are not significant regionally in many cases, but globally there is a significant increase in all scenarios. A1FI has the largest global precipitation increase overall in the 2080s, consistent with its strongest global warming signal. The mid-USA shows an increasing trend towards wetter winters (particularly in A1FI and A2 in the 2080s, though not significant in B2 or G92) but a marked trend towards drier summers (significant in all six scenarios for both periods). Southern Europe generally shows no significant change in winter precipitation apart from a significant increase in B2 by the 2080s, while in summer there is a

Table 6a Climate change signals for the globe and five selected regions for annual mean near surface temperature (K) in various HadCM3 experiments for the periods 2029–2059 (2040s) and 2069–2099 (2080s) relative to their respective 1969–1999 (1970s) period averages

Region	Period	G92	GB2	B1	B2	A2	A1FI	B2–A2	B2–GB2	Standard Deviation
Globe	2040s	1.56	1.33	1.09	1.18	1.35	1.58	–0.16	<i>–0.15</i>	0.04
	2080s	2.80	2.20	1.94	2.22	3.07	3.81	–0.85	0.01*	
Mid-USA	2040s	2.40	1.89	2.01	1.86	2.08	2.89	–0.21*	–0.03*	0.22
	2080s	4.39	3.41	3.41	3.37	4.88	6.61	–1.51	–0.03*	
S. Europe	2040s	2.12	1.67	1.53	1.79	1.74	2.20	0.05*	0.11*	0.13
	2080s	3.70	2.73	2.71	2.94	4.24	5.43	–1.30	0.21*	
Sahel	2040s	1.95	1.78	1.47	1.59	1.79	2.08	<i>–0.21</i>	–0.19*	0.07
	2080s	3.80	2.95	2.46	3.01	4.20	5.13	–1.19	0.06*	
S. Asia	2040s	1.69	1.47	1.05	1.25	1.37	1.65	–0.12*	–0.22*	0.07
	2080s	3.19	2.43	2.06	2.41	3.36	4.12	–0.95	–0.03*	
Australia	2040s	1.50	1.30	1.03	1.20	1.40	1.53	–0.20	–0.10*	0.05
	2080s	2.77	2.19	1.83	2.05	3.02	3.61	–0.97	–0.14*	

Standard deviations computed between eight successive 30-year periods from the control run are listed in the final column. Signals marked * are not significant at the 95% level assuming normality and that sampled 30-year signals from the scenario experiments have the same variance about their expected value as computed between the eight successive periods in the control run. Signals shown in *italics* are marginally significant at the 95% level. Note

that B2–GB2 represents a double difference between four independent 30-year averages, but the 1970s periods from B2 and A2 are not independent (A2 being initialized from B2 in 1989) so the same is not true for B2–A2. The variance assumed in computing the significance is adjusted for this. Regions are defined as in the IPCC 1990 and 1995 reports, e.g. Kattenberg et al. (1996)

b As Table 6a but for December–January–February (DJF) mean precipitation signals (mm/day)

Region	Period	G92	GB2	B1	B2	A2	A1FI	B2–A2	B2–GB2	Standard Deviation
Globe	2040s	0.06	0.04	0.03	0.03	0.03	0.04	0.00*	–0.01*	0.004
	2080s	0.09	0.06	0.06	0.06	0.08	0.10	<i>–0.01</i>	0.00*	
Mid-USA	2040s	0.11*	0.10*	0.11*	–0.08*	0.18	0.04*	–0.25	–0.17*	0.052
	2080s	0.12*	0.17	0.18	0.11*	0.20	0.27	–0.09*	–0.06*	
S. Europe	2040s	–0.02*	–0.06*	–0.01*	0.15*	–0.02*	0.05*	0.17*	0.21*	0.093
	2080s	0.05*	0.04*	0.08*	0.30	0.14*	0.22*	0.16*	0.26*	
Sahel	2040s	–0.01*	0.00*	–0.00*	0.00*	0.01*	–0.00*	–0.01*	0.00*	0.008
	2080s	0.00*	0.00*	–0.01*	0.01*	0.00*	–0.00*	0.01*	0.01*	
S. Asia	2040s	–0.25	–0.39	–0.19*	–0.26	–0.33	–0.11*	0.07*	0.13*	0.083
	2080s	–0.38	–0.42	–0.09*	–0.41	–0.35	–0.01*	–0.06*	0.01*	
Australia	2040s	–0.10*	–0.19*	–0.11*	–0.26*	–0.05*	0.08*	–0.21*	–0.07*	0.103
	2080s	–0.28*	–0.51	–0.13*	–0.23*	–0.20*	–0.09*	–0.02*	0.28*	

c As Table 6b but for June–July–August (JJA) mean precipitation signals (mm/day)

Region	Period	G92	GB2	B1	B2	A2	A1FI	B2–A2	B2–GB2	Standard Deviation
Globe	2040s	0.06	0.05	0.03	0.05	0.04	0.04	0.01*	0.00*	0.004
	2080s	0.08	0.06	0.06	0.07	0.08	0.09	<i>–0.01</i>	0.01	
Mid-USA	2040s	–0.13	–0.29	–0.15	–0.26	–0.18	–0.33	–0.08*	0.03*	0.033
	2080s	–0.41	–0.52	–0.11	–0.24	–0.43	–0.48	0.19	0.29	
S. Europe	2040s	–0.20	–0.27	–0.26	–0.23	–0.27	–0.33	0.04*	0.04*	0.036
	2080s	–0.43	–0.37	–0.40	–0.35	–0.51	–0.65	0.16	0.02*	
Sahel	2040s	0.21	0.17*	–0.06*	0.22	0.16*	0.16*	0.06*	0.05*	0.068
	2080s	–0.04*	–0.06*	0.04*	0.11*	0.06*	–0.05*	0.05*	0.17*	
S. Asia	2040s	0.62	0.67	0.84	0.43	0.50	0.71	–0.06*	–0.23*	0.096
	2080s	0.81	0.83	0.72	0.86	1.13	1.76	–0.27	0.03*	
Australia	2040s	–0.06*	0.08*	–0.09*	0.01*	–0.05*	–0.00*	0.06*	–0.07*	0.037
	2080s	–0.06*	–0.02*	–0.02*	–0.10*	–0.06*	–0.16	–0.04*	–0.08*	

significant drying in all six scenarios in both periods. In the Sahel, there is essentially no change in DJF precipitation at all in any scenario (the bulk of the region staying extremely dry throughout), but a more complex response in JJA with an initial tendency towards wetter summers in the 2040s, most marked in G92 and B2, subsequently reduced or reversed back to little significant change by the 2080s. Southeast Asia is the only region with generally clear and significant signals in both

seasons, namely drier in DJF and wetter in JJA in all cases, although DJF in both the B1 and A1FI scenarios shows drying signals well below the 95% significance level. The increase of 1.76 mm/day in JJA in the 2080s in A1FI is particularly noteworthy. Australia has a relatively large standard deviation in DJF precipitation in the control which makes most of the tabulated changes non-significant, but the consistent sign (apart from the 2040s in A1FI) suggests that somewhat drier conditions

are likely here in future; while in JJA no significant changes are expected in five of the six scenarios, the exception being A1FI which is significantly drier in the 2080s. In Australia, however, the regional average may obscure some significant local detail in that the monsoon response affects certain parts of the continent differently from others.

Overall, regional annual temperature and seasonal precipitation changes over the next 100 years relative to present day indicate that under the B2 scenario little difference can be expected on adding anthropogenic factors other than GHGs. This observation will not necessarily apply to other scenarios, particularly those that have stronger trends in sulfate forcing over this period. By contrast, significant differences between A2 and B2 are predicted, particularly for mid-USA and Southern Europe (both tending to larger summer drying in A2 than B2), and Southeast Asia (tending to enhanced summer monsoon, stronger in A2). It is also worth noting that for the Sahel region the initial trend towards enhanced JJA precipitation in the 2040s may be reversed by the 2080s, leading to the possibility of higher water stress under the elevated temperatures. In other regions the trends in 2040s tend to be amplified in the 2080s. As expected, the lowest emissions scenario B1 generally projects weaker responses, while the highest overall emissions scenario A1FI produces the most dramatic local warmings by the 2080s, particularly for the mid-USA region, and notably large precipitation increases in Southeast Asia in JJA, undoubtedly with implications for heightened risk of flooding.

7 Conclusions and future work

The simulations described incorporate a number of new and improved modelling features within the Hadley Centre coupled model which, we believe, taken together represent the 'state of the art', even though similar features have been adopted in some prior modelling studies. They use a set of emission scenarios derived from a self-consistent set of social and economic assumptions. They include changes in all the main greenhouse gases explicitly, some experiments including ozone trends derived using separate comprehensive models of atmospheric chemistry. Sulfate aerosol burdens have been calculated interactively in the climate model, and both the direct scattering effect of sulfate aerosols and their indirect effect on the reflectivity of water clouds have been included. The climate model includes several advances, including relatively high resolution in the ocean, allowing the model to be run without artificial flux adjustments, and improvements to the representation of the land surface.

In the B1 and B2 scenario, CO₂ emissions are lower than under IS92a, whereas in A2 and A1FI, GHG emissions eventually increase faster than in IS92a. In B1 and B2, sulfur emissions decrease throughout the twenty first century, whereas in A1FI, and especially A2, they

increase but then decrease. In all four scenarios, the global-mean forcing due to aerosols is weaker in 2100 than in 2000, although the distribution also changes. The response to the six scenarios considered differs little over the next two decades, with a rate of global-mean warming similar to that seen in recent decades. However, by the middle of the twenty first century, the global-mean warming in A1FI and A2 is noticeably greater than in B1 and B2, and by the end of the century, is greater than in IS92a (without aerosol and ozone changes). The B1 scenario, which makes relatively optimistic assumptions about limiting the future growth of emissions, warms least of all the scenarios considered but, even in this case, the average temperature rise over land areas during the twenty first century exceeds 2 K.

Global-mean sea level rise between 1900 and 2100 is predicted to be in the range 30 to 48 cm, the lower and upper values corresponding to the B1 and A1FI scenarios respectively. The largest contribution to sea level rise is from thermal expansion.

There are several pronounced differences in the modelled regional changes compared to an earlier study (MJ97): the secondary maximum of warming in the tropics is no longer present, there is a general northward shift in tropical precipitation as opposed to an in situ enhancement, and much of the northern mid-latitude continental land mass becomes drier in summer, as opposed to becoming wetter or changing little.

Analysis of regional climate change signals confirms a wide variation in annual mean warming between five land regions and across scenarios. The mid-USA has the largest warming, in the 2080s reaching 6.6 K relative to present in the A1FI scenario. There is a strong tendency for drier DJF and wetter JJA seasons in Southeast Asia through the twenty first century. In JJA, Southern Europe and mid-USA become increasingly dry in all scenarios. For the Sahel and Australia precipitation changes are less significant compared to modelled natural variability, but there are nonetheless indications of trends towards wetter conditions in the Sahel mid-century, and towards some drying in Australia at the end of the century. In DJF, the mid-USA and Southern Europe regions eventually tend to become slightly wetter while Australia becomes drier.

There are several ways in which this work could be extended or improved:

1. First, extra scenarios could be considered, and ensembles of experiments conducted for each scenario to improve the signal-to-noise ratios in the calculated responses. However, the A1 scenario is the only SRES marker scenario (Nakicenovic et al. 2000) that we have not so far considered, and it would lie within the envelope of those scenarios already performed. Therefore it may be more useful to perform ensembles of the existing scenarios instead.
2. Second, it seems likely that the sulfur burdens produced in the sulfur cycle model are too low. Improved versions of the sulfur cycle now exist (Jones et al.

2001), and will be used in future experiments. However, a bias towards low sulfur burdens may not imply a bias towards an indirect albedo forcing that is too weak, as any bias due to underestimating the anthropogenic increase in sulfate burden will be compensated to some extent by an overestimate of the susceptibility of clouds to the indirect effect. The latter arises because the natural level of aerosol burden is also underestimated, and the indirect effect depends non-linearly on this base level.

3. Third, there are considerable uncertainties in modelling the indirect effect of sulfate aerosol. The “first” indirect effect is represented here approximately and non-interactively, and the “second” indirect effect omitted. Both have been included interactively in a revised version of an atmospheric model coupled to a simple ocean (Williams et al. 2001b), but have not yet been incorporated in a fully coupled model. The second indirect effect (increasing cloud lifetimes) is likely to lead to an additional negative forcing.
4. Finally, there are a number of feedbacks and factors which have been ignored. We have not included the effect of climate change, via the increase in water vapour and oxidizing capacity of the atmosphere, on future tropospheric ozone and methane concentrations; we anticipate this would result in relatively lower concentrations than those imposed in our current simulations (i.e. a negative feedback) (Stevenson et al. 2000; Johnson et al. 2001). We have not considered feedbacks between the biosphere and climate; experiments with a related version of the model including such effects produced strong positive feedbacks (Cox et al. 2000). We have omitted the effects of changes in soot, biogenic aerosols and mineral dust. Soot is likely to give an additional warming whereas biogenic aerosols are likely to cool, but even the sign of the global mean dust forcing is not certain (Woodward 2001); although estimates of the current level of these effects exist, they are not well known and the SRES scenarios do not provide estimates of future emissions of these substances. We have also neglected land surface changes and natural forcings (solar variations and volcanoes).

There is inevitably some cancellation between the effects neglected in these experiments. However, the uncertainties associated with the individual factors are less than that accounted for by indirect aerosol forcing, which we do model, albeit imperfectly at this stage. Thus the current set of experiments provide a useful baseline against which to assess climate impacts. Future work will be directed towards assessing the individual and cumulative effects of the neglected factors on both global and regional climate as well as improving the representation of effects that we already include.

Acknowledgements This work was carried out under the UK Department of the Environment, Transport and Regions Climate Prediction Programme, DETR-CPP (PECD 7/12/37) and UK Meteorological Office Public Meteorological Service Research

Programme (MSG 2/98) with supplementary support for some experiments from the Commission of the European Communities (contract ENV4-CT95-0102 – SIDDACLICH). Supercomputing resources for this work were funded by the DETR-CPP. We thank Denise Cresswell and Gareth Jones for running the AIFI experiment, Thomas Toniazzo for running the B1 experiment, and Chris Colloff and Tristan Tuftnell for assistance with data analysis, preparing figures and tables.

Appendix A: Calibration of indirect sulfate aerosol forcing

Annual-mean distributions of sulfate aerosol were generated from HadAM3 model runs which included the sulfur cycle. Only natural emissions were used for the pre-industrial era, namely emissions of DMS (Kettle et al. 1999; Liss and Merlivat 1986) and volcanic emissions (Andres and Kasgnoc 1998). Anthropogenic emission scenarios were added to the natural emissions for the years 1860, 1900, 1950, 1975, 2000, 2050 and 2100 (see Appendix C). Successive pairs of these sulfate distributions (e.g. pre-industrial and 1860; 1860 and 1900) were then used as input to 1-year runs of HadAM3 with climatological (present-day) sea surface temperatures and sea ice. The version of HadAM3 used was identical to the atmospheric component of HadCM3 except that it used the relation of Jones et al. (1994) to predict cloud droplet number concentration (N_d) rather than the fixed N_d values used in the HadCM3 control run. Concentrations of sulfate and (over the oceans) sea-salt aerosols were used as input to this relation to determine N_d (Jones et al. 1999), subject to a minimum value of 5 cm^{-3} . For each model run the shortwave radiation scheme was called twice, once with the earlier sulfate distribution and once with the later. In each case a simple measure of cloud albedo α was calculated (Bohren 1980):

$$\alpha = \tau(1 - g)[2 + \tau(1 - g)]^{-1} \quad (1)$$

This assumes conservative scattering, and in approximating the indirect effect we also assume a fixed asymmetry parameter g ($=0.85$) and use the fact that the optical (extinction) cross section of a particle much larger than the wavelength is twice its geometrical cross section (Bohren and Huffman 1980).

For each 1-year HadAM3 model run using a pair of sulfate scenarios, the distribution of the change in α caused by the changes in aerosol was stored and used to build up a history of the change in cloud albedo ($\Delta\alpha$). If dx_1, dx_2 etc. represent the changes in cloud albedo for the sulfate distributions pairs {pre-industrial,1860}, {1860, 1900} etc. respectively, then the cloud albedo change at each “marker” year is calculated by summation:

$$\begin{aligned} \Delta\alpha(1860) &= dx_1 \\ \Delta\alpha(1900) &= dx_1 + dx_2 \\ &\text{etc.} \end{aligned}$$

Cloud albedo changes between these dates were obtained by linear interpolation.

These cloud albedo changes were used to simulate indirect forcing in the HadCM3 runs as follows. The change in α due to the change in aerosol distribution corresponds to changing τ by a factor λ :

$$\Delta\alpha = \lambda\tau(1 - g)[2 + \lambda\tau(1 - g)]^{-1} - \tau(1 - g)[2 + \tau(1 - g)]^{-1} \quad (2)$$

Re-arranging Eq. (1) to give an expression for τ and then substituting into Eq. (2) yields:

$$\Delta\alpha = \lambda\alpha[(1 - \alpha) + \lambda\alpha]^{-1} - \alpha \quad (3)$$

Following Platnick and Twomey (1994), we define a factor χ , the fractional change of N_d corresponding to the fractional change λ in τ . As τ is inversely proportional to the cloud droplet effective radius r_e , and as r_e is proportional to $N_d^{-1/3}$ (Martin et al. 1994), then we can replace λ by $\chi^{1/3}$. Re-arranging Eq. (3) then gives:

$$\chi = [\Delta\alpha(\alpha - 1) - \alpha(1 - \alpha)]^3 [\alpha(\Delta\alpha + \alpha - 1)]^{-3} \quad (4)$$

At each time step in the HadCM3 run the fixed values of N_d and the predicted cloud water content were used to derive an initial value for r_e using the parametrization of Martin et al. (1994). Cloud optical depth τ was then calculated and used to derive an initial distribution of α using Eq. (1). The distribution of $\Delta\alpha$ for the appropriate time was available from the offline history produced from the HadAM3 runs and used in conjunction with α to calculate χ using Eq. (4). Note that at this point in the model r_e has only been used to determine the initial distribution of α . Before r_e was used in the radiation code for a full calculation of cloud radiative properties it was modified to r_e' using χ to approximate the indirect albedo effect:

$$r_e' = r_e \chi^{-1/3} \quad (5)$$

It is possible for χ to be infinite, zero or negative, implying either: (1) that the decrease in cloud albedo required is greater than ($\chi < 0$) or equal to ($\chi = 0$) the current value of α , and in such cases the cloud was made as dark as possible by setting r_e to the maximum value allowed ($37 \mu\text{m}$); or (2) that the increase in cloud albedo required to produce the desired forcing, when added to α , produces a result which is greater than ($\chi < 0$) or equal to ($\chi \rightarrow \infty$) unity, and in such cases the cloud was made as bright as possible by setting r_e to the minimum permitted value ($0.35 \mu\text{m}$). Both these factors may exert a limiting influence on the forcing actually produced in the coupled run, as may differences between the cloud distribution of the coupled run and of the atmosphere-only runs used to generate the albedo-change history. It is too computationally expensive to calculate the actual forcing experienced by the coupled model as the simulation evolves as this would require multiple calls to the (computationally intensive) radiation scheme. Consequently, 1-year portions of the simulations were re-run with extra radiation calls and diagnostics for the scenario years 1860, 1900, 1950, 1975, 2000, 2050 and 2100. The ideal forcing for these years was available from the separate HadAM3 runs used to generate the albedo-change history, and this was compared with the actual forcing produced in HadCM3 in these years.

Appendix B: Calculation of ozone trends

In the troposphere the ozone trends are constructed by means of off-line 3-D chemical transport (STOCHEM, Collins et al. 1997, 1999) model simulations for specific epochs 1990, 2030, 2060 and 2100; each simulation being run for 15 months. Intermediate results are obtained by linear interpolation in time. Initial methane concentrations are provided from an earlier run of the 2-D TROPOS model. Emissions for 1990 are based on those from the EDGAR database (Olivier et al. 1996), with future emissions taken from the SRES scenario definitions themselves. The 3-D STOCHEM model runs are also meteorologically and dynamically forced with six-hourly data from a previous HadCM3 coupled experiment which to first order reflects the climate conditions (e.g. global warming) expected at the appropriate time.

All SRES scenarios assume the Montreal protocol is followed, the Cl and Br concentrations being determined via box modelling techniques. The resulting stratospheric ozone concentrations are then scenario-independent. For the purpose of extrapolating stratospheric ozone depletion into the future, ‘effective equivalent stratospheric chlorine’ ($\text{EESC} = \text{Cl} + 40 \cdot \text{Br}$) contributions were estimated for Cl and Br compounds not already included in the 2-D model used for computing well-mixed minor GHGs by means of a simple box model driven using SRES and natural emissions where appropriate. Tropospheric mixing ratio estimates from this and the 2-D model for years from 1950 to 2100 were then combined and used to calculate stratospheric ozone as a function of height, longitude and month, assuming:

1. That it takes 3 years for tropospheric Cl and Br to get into the stratosphere
2. That ozone is depleted linearly by EESC levels above the 1974 stratospheric level, any implied negative ozone values being replaced by a minimum ozone mass mixing ratio of 10^{-11} for numerical reasons

Ozone loss is at its largest in 2002 and recovers subsequently as EESC returns to preindustrial values. Beyond about 2060, this should have resulted in a stabilization of stratospheric ozone at preindustrial levels again, but due to a software error ozone in fact continued to increase. This leads to an erroneous small positive net forcing of $+0.17 \text{ W/m}^2$ from stratospheric ozone at 2100 relative to preindustrial in all the scenarios. Further details of the method and the stratospheric ozone trends up to present day is given by Tett et al. (2002). Zero ozone change was imposed at the tropopause model level, as estimated from the 1871–1990 mean tropopause height of a HadAM3 integration forced by the observed sea surface temperatures and sea ice extents from the GISST3.1 data set, an updated version of that described in Rayner et al. (1996).

Appendix C: Anthropogenic sulfur emissions

Only anthropogenic emissions were included in the experiments. For the ‘past’ portion of the experiments, the basic datasets we used are the revised version of the 1985 GEIA 1B dataset (released in June 1997 – see <http://www.geiacenter.org/> and <http://www.ortech.ca/cgeic> for details) and the University of Stockholm (Orn et al. 1996) historic emissions datasets for 1860, 1870, ... 1970. The GEIA 1B dataset includes seasonal variations over some regions, e.g. Europe, but for convenience we employed an annually averaged version. In any case the Stockholm datasets are annual means. The GEIA 1B dataset also splits the emissions into those from near-surface and elevated sources such as power station chimneys; the latter were injected into the third model level above the surface (approximately 550–1000 m), to allow for buoyant plume rise.

For the ‘future’ portion of the experiments, we used the preliminary versions of two of the four possible marker scenarios produced by the IPCC SRES group, namely A2 and B2. We also used the published versions of the ‘fossil fuel intensive’ variant of the A1 scenario (known as A1FI) and the B1 marker scenario, both of which were developed at a later stage (Nakicenovic et al. 2000).

The SRES SO_2 emissions are provided on a regular latitude–longitude grid at a resolution of $1^\circ \times 1^\circ$. Fields are available at ten year intervals from 1990 to 2100. Note that the emissions actually used at 1990 in the HadCM3 experiments B1 and A1FI were identical to those in A2 for simplicity in conducting the experiments, rather than the slightly different values tabulated in Table 2 which reflect revisions between the preliminary and final versions of the respective emissions scenarios. The complete sequence of base dates, between which emissions are found by interpolation, is therefore 1860, 1870, ... 1980, 1985, 1990, 2000, 2010, ... 2090, 2100.

Define a two-dimensional field \mathcal{F} by

$$\mathcal{F}(x, y) = \frac{H(x, y, 1985)}{H(x, y, 1985) + S(x, y, 1985)}$$

where $H(x, y, 1985)$ is the GEIA 1B elevated emission field and $S(x, y, 1985)$ is the GEIA 1B surface emission field. \mathcal{F} is thus the fraction of the emissions from elevated sources. (Where there are no emissions in 1985 \mathcal{F} is set to zero.) \mathcal{F} was used to split the Stockholm historic datasets into surface and elevated components. Clearly the fraction of emissions from elevated sources has varied in time, so introduce a factor $\phi(t)$ to describe this: assume that $\phi(t)$ is zero before 1950, 1 after 1985 and varies linearly with time between 1950 and 1985. Emissions prior to 1985 were thus split by multiplying them by $\phi(t)$ $\mathcal{F}(x, y)$ to generate an elevated source dataset, the remaining emissions being assigned to the surface source field.

We have no information about possible changes in \mathcal{F} in the future, so we assumed that no changes take place after 1985. This is not ideal, because it is clear that changes will occur, and the emission height does affect the sulfate distribution.

References

- Allen MR, Ingram WJI (2002) Constraints on future changes in climate and the hydrological cycle. *Nature* 419:224–232
- Albrecht BA (1989) Aerosols, cloud microphysics and fractional cloudiness. *Science* 245: 1227–1230
- Andres RJ, Kasgnoc AD (1998) A time-averaged inventory of subaerial volcanic sulfur emissions. *J Geophys Res* 103: 25,251–25,261
- Barnett TP, Hasselmann K, Chelliah M, Delworth T, Hegerl G, Jones P, Rasmussen E, Roeckner E, Ropelewski C, Santer B, Tett S (1999) Detection and attribution of climate change: a status report. *Bull Am Meteorol Soc* 12: 2631–2659
- Boer GJ (1993) Climate change and the regulation of the surface moisture and energy budgets. *Clim Dyn* 8: 225–239
- Bohren CF (1980) Multiple scattering of light and some of its observable consequences. *Am J Phys* 55: 524–533
- Bohren CF, Huffman DR (1983) Absorption and scattering of light by small particles. John Wiley and Sons, New York, pp 530
- Boville BA, Gent PR (1998) The NCAR Climate System Model, version one. *J Clim* 11: 1115–1130
- Boville BA, Kiehl JT, Rasch PJ, Bryan FO (2001) Improvements to the NCAR CSM-1 for transient climate simulations. *J Clim* 14: 164–179
- Bower KN, Choulaton TW (1992) A parametrization of the effective radius of ice free clouds for use in global climate models. *Atmos Res* 27: 305–339
- Cattle H, Crossley J (1995) Modelling Arctic climate change. *Philos Trans R Soc London A352*: 201–213
- Collins M, Tett SFB, Cooper C (2001) The internal climate variability of HadCM3, a version of the Hadley Centre coupled model without flux adjustments. *Clim Dyn* 17: 61–81
- Collins WJ, Stevenson DS, Johnson CE, Derwent RG (1997) Tropospheric ozone in global-scale three-dimensional model and its response to NO_x emission controls. *J Atmos Chem* 26: 223–274
- Collins WJ, Stevenson DS, Johnson CE, Derwent RG (1999) The role of convection in determining the budget of odd hydrogen in the upper troposphere. *J Geophys Res* 104: 26,927–26,941
- Cox P, Betts R, Bunton C, Essery R, Rowntree PRR, Smith J (1999) The impact of new land surface physics on the GCM simulation of climate and climate sensitivity. *Clim Dyn* 15: 183–203
- Cox PM, Betts RA, Jones CD, Spall SA, Totterdell IJ (2000) Acceleration of global warming by carbon cycle feedbacks in a 3D coupled model. *Nature* 408: 184–187
- Cubasch U, Meehl GA, Boer GJ, Stouffer RJ, Dix M, Noda A, Senior CA, Raper S, Yap KS (2001) Projections of Future Climate Change. In: Houghton JT, Ding Y, Griggs DJ, Noguer M, van der Linden PJ, Dai X, Maskell K, Johnson CA (eds) *Climate change 2001. The scientific basis. Contribution of Working Group I to the Third Assessment Report of the Intergovernmental Panel on Climate Change*. Cambridge University Press, Cambridge, UK, pp 881
- Cusack S, Slingo A, Edwards JM, Wild M (1998) The radiative impact of a simple aerosol climatology on the Hadley Centre GCM. *Q J R Meteorol Soc* 124: 2517–2526
- Dai A, Wigley TML, Boville BA, Kiehl JT, Buja LE (2001) Climates of the 20th and 21st centuries simulated by the NCAR Climate System Model. *J Clim* 14: 485–519
- Edwards JM, Slingo A (1996) Studies with a flexible new radiation code. I: choosing a configuration for a large scale model. *Q J R Meteorol Soc* 122: 689–719
- Fitzgerald JW (1975) Approximation formulas for the equilibrium size of an aerosol particle as a function of its dry size and composition and the ambient relative humidity. *J Appl Meteorol* 14: 1044–1049
- Forster PM de F, Shine KP (1997) Radiative forcing and temperature trends from stratospheric ozone changes. *J Geophys Res* 102: 10,841–10,855
- Gent PR, McWilliams JC (1990) Isopycnal mixing in ocean circulation models. *J Phys Oceanogr* 20: 150–155
- Gordon C, Cooper C, Senior CA, Banks HT, Gregory JM, Johns TC, Mitchell JFB, Wood RA (2000) The simulation of SST, sea ice extents and ocean heat transports in a version of the Hadley Centre coupled model without flux adjustments. *Clim Dyn* 16: 147–168
- Gregory D, Rowntree PR (1990) A mass flux convection scheme with representation of ensemble characteristics and stability dependent closure. *Mon Weather Rev* 118: 1483–1506
- Gregory D, Kershaw R, Inness PM (1997) Parametrization of momentum transport by convection. II: tests in single column and general circulation models. *Q J R Meteorol Soc* 123: 1153–1183
- Gregory D, Shutts GJ, Mitchell JR (1998) A new gravity wave drag scheme incorporating anisotropic orography and low level wave breaking: impact upon the climate of the UK Meteorological Office Unified Model. *Q J R Meteorol Soc* 124: 463–493
- Gregory JM, Lowe JA (2000) Predictions of global and regional sea-level rise using AOGCMs with and without flux adjustment. *Geophys Res Lett* 27: 3069–3072
- Gregory JM, Church JA, Boer GJ, Dixon KW, Flato GM, Jackett DR, Lowe JA, O'Farrell SP, Roeckner E, Russell GL, Stouffer RJ, Winton M (2001) Comparison of results from several AOGCMs for global and regional sea-level change 1900–2100. *Clim Dyn* 18: 225–240
- Hough AM (1991) Development of a two-dimensional global tropospheric model: model chemistry. *J Geophys Res* 96: 7325–7326
- Houghton JT, Jenkins GJ, Ephraums JJ (eds) (1990) *Climate change: the IPCC scientific assessment*. Cambridge University Press, Cambridge, UK, pp 365
- Houghton JT, Meira Filho LG, Bruce J, Lee H, Callander BA, Haites E, Harris N, Maskell K (eds) (1996) *Climate change 1995: the science of climate change*. Cambridge University Press, Cambridge, UK, pp 572
- Houghton JT, Ding Y, Griggs DJ, Noguer M, van der Linden PJ, Dai X, Maskell K, Johnson CA (eds) (2001) *Climate change 2001. The scientific basis. Contribution of Working Group I to the Third Assessment Report of the Intergovernmental Panel on Climate Change*. Cambridge University Press, Cambridge, UK, pp 881
- Hulme M, Jenkins GJ (1998) *Climate change scenarios for the United Kingdom*. UK Climate Impacts Programme Tech Note 1, (61 + xv)pp
- Hulme M, Mitchell JFB, Ingram WJ, Johns TC, New M, Viner D (1999) *Climate change scenarios for global impact studies*. *Global Environ Change* 9: S3–S19
- Johns TC, Carnell RE, Crossley JF, Gregory JM, Mitchell JFB, Senior CA, Tett SFB, Wood RA (1997) The Second Hadley Centre Coupled Ocean–Atmosphere GCM: model description, spinup and validation. *Clim Dyn* 13: 103–134
- Johnson CE, Collins WJ, Stevenson DS, Derwent RG (1999) Relative roles of climate and emissions changes on future tropospheric oxidant concentrations. *J Geophys Res* 104: 18,631–18,645
- Johnson CE, Stevenson DS, Collins WJ, Derwent RG (2001) Role of climate feedback on methane and ozone studied with a coupled ocean–atmosphere–chemistry model. *Geophys Res Lett* 28: 1723–1726
- Jones A, Roberts DL, Slingo A (1994) A climate model study of indirect radiative forcing by anthropogenic sulphate aerosols. *Nature* 370: 450–453
- Jones A, Roberts DL, Woodage MJ (1999) The indirect effects of anthropogenic sulphate aerosol simulated using a climate model with an interactive sulphur cycle. Hadley Centre Technical Note 14, Met Office, Bracknell, UK, pp 39
- Jones A, Roberts DL, Woodage MJ, Johnson CE (2001) Indirect sulphate aerosol forcing in a climate model with an interactive sulphur cycle. *J Geophys Res* 106 D17: 20,293–20,310
- Joos F, Bruno M, Fink R, Siegenthaler U, Stocker T, Le Quéré C, Sarmiento JL (1996) An efficient and accurate representation of complex oceanic and biospheric models of anthropogenic carbon uptake. *Tellus* 48B: 397–417

- Kattenberg A, Georgi F, Grassl H, Meehl GA, Mitchell JFB, Stouffer RJ, Tokioka T, Weaver AJ, Wigley TML (1996) Climate models – projections of future climate. In: Houghton JT, Meira Filho LG, Callander BA, Harris N, Kattenberg A, Maskell K (eds) *Climate change 1995. The science of climate change*. Cambridge University Press, Cambridge, UK, pp 572
- Kettle AJ, Andreae MO, Amouroux D, Andreae TW, Bates TS, Berresheim H, Bingemer H, Boniforti R, Helas G, Leck C, Maspero M, Matrai P, McTaggart AR, Mihalopoulos N, Nguyen BC, Novo A, Putaud JP, Rapsomanikas S, Roberts G, Schebeske G, Sharma S, Simo R, Staubes R, Turner S, Uher G (1999) A global database of sea surface dimethylsulfide (DMS) measurements and a procedure to predict sea surface DMS as a function of latitude, longitude and month. *Global Biogeochem Cycles* 13: 399–444
- Kraus EB, Turner JS (1967) A one dimensional model of the seasonal thermocline. Part II. *Tellus* 19: 98–105
- Levitus S, Boyer TP (1994) *World Ocean Atlas 1994, vol 4: temperature*. NOAA/NESDIS E/OC21, US Department of Commerce, Washington DC, pp 117
- Levitus S, Burgett R, Boyer TP (1995) *World Ocean Atlas 1994, Vol 3: salinity*. NOAA/NESDIS E/OC21, US Department of Commerce, Washington DC, pp 99
- Li D, Shine KP (1995) A 4-dimensional ozone climatology for UGAMP models. UGAMP Internal Report 35
- Liss PS, Merlivat L (1986) Air–sea gas exchange rates: introduction and synthesis. In: Buat-Menard P (ed) *The role of air–sea exchange in geochemical cycling*. Reidel, Dordrecht, Netherlands
- Mahlman JD (2001) Projections of future changes in climate. In: MacCracken MC, Perry JS (eds) *Encyclopaedia of global environmental change, vol 1*. John Wiley, Chichester, UK, pp 688
- Manabe S, Wetherald RT (1975) The effect of doubling CO₂ concentrations on the climate of a GCM. *J Atmos Sci* 32: 3–15
- Martin GM, Johnson DW, Spice A (1994) The measurement and parametrization of effective radius of droplets in warm stratocumulus clouds. *J Atmos Sci* 51: 1823–1842
- Milton SF, Wilson CA (1996) The impact of parametrized sub-grid scale orographic forcing on systematic errors in a global NWP model. *Mon Weather Rev* 124: 2023–2045
- Mitchell JFB, Johns TC (1997) On modification of global warming by sulphate aerosols. *J Clim* 10: 245–267
- Mitchell JFB, Johns TC, Senior CA (1999) Transient response to increasing greenhouse gases using models with and without flux adjustments. Hadley Centre Technical Note 2, Met Office, Bracknell, 15pp + 20 figs
- Mitchell JFB, Karoly DJ, Hegerl GC, Zwiers FW, Allen MR, Marengo J (2001) Detection of climate change and attribution of causes. In: Houghton JT, Ding Y, Griggs DJ, Noguer M, van der Linden PJ, Dai X, Maskell K, Johnson CA (eds) *Climate change 2001. The scientific basis. Contribution of Working Group I to the Third Assessment Report of the Intergovernmental Panel on Climate Change*. Cambridge University Press, Cambridge, UK, USA, pp 881
- Murphy JM, Mitchell JFB (1995) Transient response of the Hadley Centre coupled ocean atmosphere model to increasing carbon dioxide. Part II: spatial and temporal structure of response. *J Clim* 8: 57–80
- Nakicenovic N, and 27 co-authors (2000) *IPCC Special report on emission scenarios*. Cambridge University Press, Cambridge, UK, pp 599
- Noda A, Yukimoto S, Maeda S, Uchiyama T, Shibata K, Yamaki S (2001) A New Meteorological Research Institute Coupled GCM (MRI-CGCM2) Transient response to greenhouse gas and aerosol scenarios. Centre for Global Environmental Research Report, NIES, Japan, pp 63
- Nozawa T, Emori S, Numagati A, Tsushima Y, Takemura T, Nakajima T, Abe-Ouchi A, Kimoto M (2001) Projections of future climate change in the 21st century simulated by the CCSR/NIES CGCM under the IPCC SRES scenarios. In: Matsuno T, Kida H (eds) *Present and future of modelling global environment change – toward integrated modelling*. Terra Scientific, Tokyo, Japan, pp 15–28
- Olivier JGJ, Bouwman AF, van der Maas CWM, Berdowski JJM, Veldt C, Bloos JPJ, Visschedijk AJH, Zandveld PYK, Haverlag JL (1996) Description of EDGAR Version 2.0: a set of global emission inventories of greenhouse gases and ozone-depleting substances for all anthropogenic and most natural sources on a per country basis and on a 1 deg x 1 deg grid. National Institute of Public Health and the Environment, The Netherlands. RIVM Rep 771060 002, TNO-MEP Rep R96/119, pp 141
- Orn G, Hansson U, Rodhe H (1996) Historical worldwide emissions of anthropogenic sulfur: 1860–1985. International Meteorological Institute in Stockholm, Rep CM-91, Stockholm University, 5pp + 15 plates
- Pacanowski RC, Philander SG (1981) Parametrization of vertical mixing in numerical models of tropical oceans. *J Phys Oceanogr* 11: 1443–1451
- Parker DE, Jones PD, Folland CK, Bevan A (1994) Interdecadal changes of surface temperature since the late nineteenth century. *J Geophys Res* 99: 14,373–14,399
- Penner JE, Andreae M, Annegarn H, Barrie L, Feichter J, Hegg D, Jayaraman A, Leaitch R, Murphy D, Nganga J, Pitari G (2001) Aerosols, their direct and indirect effects. In: Houghton JT, Ding Y, Griggs DJ, Noguer M, van der Linden PJ, Dai X, Maskell K, Johnson CA (eds) *Climate change 2001. The scientific basis. Contribution of Working Group I to the Third Assessment Report of the Intergovernmental Panel on Climate Change*. Cambridge University Press, Cambridge, UK, pp 881
- Platnick S, Twomey S (1994) Determining the susceptibility of cloud albedo to changes in droplet concentration with the advanced very high resolution radiometer. *J Appl Meteorol* 33: 334–347
- Pope VD, Gallani ML, Rowntree PR, Stratton RA (2000) The impact of new physical parametrizations in the Hadley Centre climate model: HadAM3. *Clim Dyn* 16: 123–146
- Prather M, Ehhalt D, Dentener F, Derwent R, Dlugokencky E, Holland E, Isaksen I, Katima J, Kirchhoff V, Matson P, Middleby P, Wang M (2001) Atmospheric chemistry and greenhouse gases. In: Houghton JT, Ding Y, Griggs DJ, Noguer M, van der Linden PJ, Dai X, Maskell K, Johnson CA (eds) *Climate change 2001. The scientific basis. Contribution of Working Group I to the Third Assessment Report of the Intergovernmental Panel on Climate Change*. Cambridge University Press, Cambridge, UK, pp 881
- Ramanathan V, Dickinson RE (1979) The role of stratospheric ozone in the zonal and seasonal radiative energy balance of the Earth–troposphere system. *J Atmos Sci* 36: 1084–1104
- Ramaswamy V, Boucher O, Haigh J, Hauglustaine D, Haywood J, Myhre G, Nakajima T, Shi GY, Solomon S (2001) Radiative forcing of climate change. In: Houghton JT, Ding Y, Griggs DJ, Noguer M, van der Linden PJ, Dai X, Maskell K, Johnson CA (eds) *Climate change 2001. The scientific basis. Contribution of Working Group I to the Third Assessment Report of the Intergovernmental Panel on Climate Change*. Cambridge University Press, Cambridge, UK, pp 881
- Rayner NA, Horton EB, Parker DE, Folland CK, Hackett RB (1996) Version 2.2 of the Global sea-Ice and Sea Surface Temperature dataset, 1903–1994. Climate Research Technical Note 74, Met Office, Bracknell, UK, 21pp + 13 figs
- Roegner E, Bengtsson L, Feichter J, Lelieveld J, Rodhe H (1999) Transient climate change simulations with a coupled atmosphere–ocean GCM including the tropospheric sulfur cycle. *J Clim* 12: 3004–3032
- Roether W, Roussinov VM, Well R (1994) A tracer study of the thermohaline circulation of the eastern Mediterranean. In: Malanotte-Rizzoli P, Robinson AR (eds) *Ocean processes in climate dynamics: global and Mediterranean example*. Kluwer Academic, pp 371–394
- Santer BD, Wigley TML, Barnett TP, Anyamba E (1996) Detection of Climate Change and Attribution of Causes. In: Houghton JT, Meira Filho LG, Callander BA, Harris N, Kattenberg A, Maskell K (eds) *Climate change 1995. The science of climate change*. Cambridge University Press, Cambridge, UK, pp 572

- Schimel D, and 26 co-authors (1996) Radiative forcing of climate change. In: Houghton JT, Meira Filho LG, Callander BA, Harris N, Kattenberg A, Maskell K (eds) *Climate change 1995. The science of climate change*. Cambridge University Press, Cambridge, UK, pp 572
- Shine KP, Derwent RG, Wuebbles DJ, Morcrette J-J (1990) Radiative forcing of climate. In: Houghton JT, Jenkins GJ, Ephraums JJ (eds) *Climate change. The IPCC scientific assessment*. Cambridge University Press, Cambridge, UK, pp 365
- Smith RNB (1990) A scheme for predicting layer clouds and their water content in a general circulation model. *Q J R Meteorol Soc* 116: 435–460
- Stendel M, Schmith T, Roeckner E, Cubasch U (2000) The climate of the 21st century: transient simulations with a coupled atmosphere–ocean general circulation model. *Danmarks Klimacenter Report 00-6*, Danish Meteorological Institute, Copenhagen, Denmark, pp 51
- Stevenson DS, Johnson CE, Collins WJ, Derwent RG, Edwards JM (2000) Future estimates of tropospheric ozone radiative forcing and methane turnover – the impact of climate change. *Geophys Res Lett* 27: 2073–2076
- Stott PA, Tett SFB, Jones GS, Allen MR, Ingram WJ, Mitchell JFB (2001) Attribution of twentieth century temperature change to natural and anthropogenic causes. *Clim Dyn* 17: 1–21
- Tett SFB, Stott PA, Allen MR, Ingram WJ, Mitchell JFB (1999) Causes of twentieth century temperature change. *Nature* 399: 569–572
- Tett SFB, Jones GS, Stott PA, Hill D, Mitchell JFB, Allen MR, Ingram WJ, Johns TC, Johnson CE, Jones A, Roberts DL, Sexton DMH, Woodage MJ (2002) Estimation of natural and anthropogenic contributions to 20th century climate temperature change. *J Geophys Res* 107 (D16), 10.1029/2000JD000028
- Toon OB, Pollack JB, Khare BN (1976) The optical constants of several atmospheric aerosol species: ammonium sulfate, aluminium oxide, and sodium chloride. *J Geophys Res* 81: 5733–5748
- US National Assessment synthesis team (2000) *Climate change impacts on the United States*. US Global Change Programme, Cambridge University Press, pp 154
- Visbeck M, Marshall J, Haine T, Spall M (1997) On the specification of eddy transfer coefficients in coarse resolution ocean circulation models. *J Phys Oceanogr* 27: 381–402
- Wang HJ, Cunnold DM, Bao X (1996) A critical analysis of stratospheric aerosol and gas experiment ozone trends. *J Geophys Res* 101 D7: 12,495–12,514
- Williams KD, Senior CA, Mitchell JFB (2001a) Transient climate change in the Hadley Centre models: the role of physical processes. *J Clim* 14: 2659–2674
- Williams KD, Jones A, Roberts DL, Senior CA, Woodage MJ (2001b) The response of the climate system to the indirect effects of anthropogenic sulfate aerosol. *Clim Dyn* 17: 845–856
- Wood RA, Keen AB, Mitchell JFB, Gregory JM (1999) Changing spatial structure of the thermohaline circulation in response to atmospheric CO₂ forcing in a climate model. *Nature* 399: 572–575
- Woodward S (2001) Modelling the atmospheric life cycle and radiative impact of mineral dust in the Hadley Centre climate model. *J Geophys Res* 106: 18,155–18,166
- Wright DK (1997) A new eddy mixing parametrization and ocean general circulation model. *International WOCE News* 26: 27–29
- Xie P, Arkin PA (1997) Global precipitation: a 17-year monthly analysis based on gauge observations, satellite estimates and numerical model outputs. *Bull Am Meteorol Soc* 78: 2539–2558